

# Estimation and prediction of shallow ground source heat resources subjected to complex soil and atmospheric boundary conditions

Wu Gao<sup>\*</sup>, Shakil Masum, Meysam Qadrdan, Hywel Rhys Thomas

School of Engineering, Cardiff University, The Queen's Building, The Parade, Cardiff, CF24 3AA, United Kingdom

## ARTICLE INFO

### Keywords:

Shallow ground source heat  
Ground temperature  
Thermo-hydraulic model  
Soil-atmosphere interface  
Heat content

## ABSTRACT

5th generation district heating and cooling networks operating at near ground temperature offer a low-cost, zero-carbon energy solution. Detailed understanding and accurate estimation of ground behaviour for its heat storage and recharge potential are of paramount importance for the success of such networks. In this paper, an advanced modelling tool, based on a coupled Thermal-Hydraulic (TH) modelling framework, is presented to calculate and predict temperature and soil-moisture behaviour of a shallow ground under complex atmospheric, temperature and hydraulic boundary conditions. Atmospheric data e.g., solar radiation, rainfall, humidity, air temperature, wind velocity is considered together with subsurface soil data to investigate thermal and hydraulic responses of the ground, and its individual soil layers. Furthermore, a transient method for estimating shallow ground source heat (SGSH) resources is proposed based on the simulated temperature and saturation distributions of the ground. The model is applied to predict the long-term ground temperature and saturation level of a test site located in Warwickshire County, UK. The total heat content per unit area and the annual/seasonal/monthly net heat content per unit area of the site are predicted for a five-year period. The total heat content of the sandy clay layer varied between 2.32 and 11.6 MJ/m<sup>2</sup>, silty clay from 34.0 to 50.5 MJ/m<sup>2</sup>, and mudstone from 50.7 to 55.0 MJ/m<sup>2</sup>. A parametric sensitivity study is also conducted to investigate the effects of soil types and hydraulic drainage conditions on the ground heat supply potential, and it revealed that the spatial and temporal distributions of ground heat is significantly affected by the underlying soils. This study highlights the influences of atmospheric conditions and coupled ground processes, and the parameters that should be considered for designing a 5th generation low-temperature heat network.

## 1. Introduction

Great ambitions on Climate Change, such as the Glasgow Climate Pact and the Paris Agreement to limit the global temperature rise to 1.5 °C above pre-industrial levels [1], and the European Green Deal to achieve no net emissions of greenhouse gases (GHG) by 2050 [2], require significant reduction of fossil fuel usage and promotion of zero-carbon, renewable energy solutions. Energy sector is one of the largest emitters of GHG, dominated by space heating and cooling demand. The International Energy Agency (IEA) reported that half of the global energy consumption is associated with heating homes, industries, and other applications [3]. Heating and cooling accounted for 40% of the overall energy use in Europe [4] and heating alone accounted for 44% of the total energy consumption (in the year 2017) in the United Kingdom [5]. Meanwhile, the warmer summer periods have accelerated the cooling demand in recent years. Therefore, decarbonisation of the

heating and cooling systems is essential to reduce GHG emission and to achieve a net-zero energy sector in Europe and across the globe.

Numerous efforts are ongoing to decarbonise heating, including exploitation of geothermal energy, solar energy, waste heat, combined heat and power (CHP) plants, etc. [6–9]. These low carbon heating options can be integrated, individually or collectively, to form heat networks, i.e., district heating and cooling networks (DHC). The DHCs are recognised for their effectiveness in reducing fossil fuel or primary energy consumption and associated emissions [8]. The conventional heating networks, based on high temperature CHP systems, yet requires significant input from fossil fuels, but the 4th and 5th generation district heating and cooling systems operate at the low temperature and even the near-ambient/ground temperature, and offer a low-cost, zero carbon supply of heating and cooling with flexibility of integrating other renewable energy sources [10].

Geothermal energy, such as shallow ground source heat (SGSH)

<sup>\*</sup> Corresponding author.

E-mail addresses: [gaow11@cardiff.ac.uk](mailto:gaow11@cardiff.ac.uk), [gaowu\\_ed@163.com](mailto:gaowu_ed@163.com) (W. Gao).

<https://doi.org/10.1016/j.renene.2022.07.148>

Received 21 February 2022; Received in revised form 28 June 2022; Accepted 29 July 2022

Available online 11 August 2022

0960-1481/© 2022 The Authors. Published by Elsevier Ltd. This is an open access article under the CC BY license (<http://creativecommons.org/licenses/by/4.0/>).

energy [11,12], is becoming increasingly popular for heating and cooling of residential, commercial, and public buildings [13], and it is aligned with the development of the 5th generation heating and cooling networks.

To support design and installation of ground source heat pump (GSHP) for exploiting SGSH for a 5th generation network, the amount of thermal energy available in a ground should be thoroughly investigated. If the reserves of SGSH cannot meet the demand, GSHP can be combined with other systems, such as solar thermal panels, to create hybrid systems for greater performance [13–15]. To estimate ground temperatures accurately, it is essential to understand dynamics of ground thermal behaviour which varies seasonally, with soil types and covers, and with atmospheric conditions, such as precipitation, condensation, evaporation etc. [11,12,16–18].

Reserves of SGSH are closely related to ground temperature distribution and heat fluxes through the soil-atmosphere interface [11,12]. Research has studied temperature profiles and heat fluxes in shallow grounds. Oliver et al. [16] measured soil temperature and soil heat fluxes from several sites in the U.K. and Syria, and they reported that daily soil heat fluxes could be estimated reasonably from soil temperatures. Mihalakakou et al. [19] proposed a mathematical model based on the transient heat conduction equation and the energy balance equation, which was used to predict ground surface temperature of bare and short-grass covered soils. They validated their model against experimental data obtained from Athens and Dublin and found that the surface temperatures were sensitive to wind speed, soil absorptivity, evaporation, and relative humidity. Staniec and Nowak [20] predicted annual soil temperature distributions via a mathematical model, which was also based on the transient heat conduction equation with energy balance at the soil surface boundary. From sensitivity studies they revealed that the model was mostly sensitive to changes of air temperature. Bryś et al. [11] gathered nine-years of temperature and radiation data of bare soil and grassy soil in Poland. Annual and monthly variabilities of positive heat flux density at various locations of a subsurface shallow depth soil layer (SSDSL) were analysed based on the energy balance equation. In a follow-up study, Bryś et al. [12] investigated the dynamics of diurnal, monthly, seasonal, and annual positive and negative heat fluxes in SSDSL based on ten-year measured data of bare soil and grassy soil in Poland. Factors affecting the energy balance equation and thermal reserves of SSDSL were discussed.

Existing models predicting soil temperature are often confronted with limitations. For example, they are applicable only to certain meteorological conditions [21], simplified in nature, and often neglect coupled thermo-hydraulic behaviours of a ground [19–21]. In the aforementioned studies, soil temperature and heat fluxes were analysed primarily from the perspective of energy balance. However, soil is a three-phase system consisting of solid aggregates, pore-water, and pore-air. Heat and moisture exchange occur constantly through the soil-atmosphere interface and soil thermal behaviours depend on responses of these constituents, both individually and collectively. For example, thermal properties of soils are influenced by its water content [17,18]. Saturated soils with water-filled pores facilitate higher thermal conductivity than partially or unsaturated soils, where the pore spaces are occupied by both water and air. Akrouh et al. [22] conducted experimental investigation into sandy soil and observed that the thermal conductivity reduced from 2.65 W/m/K in saturated condition to 0.9 W/m/K in dry soil. To obtain reasonable temperature and heat flux, as well as to calculate the key GSHP parameters, e.g., loop length, heat exchange efficiency, and heat loss, it is essential to investigate the coupled thermo-hydraulic (TH) behaviour of the ground including the complexities of variable climatic conditions [23]. This is a pre-requisite for accurate design and estimation of an effective and efficient low-temperature heat network.

In this paper, dynamic thermal and hydraulic behaviours of a ground that is subjected to complex atmospheric conditions are investigated for shallow ground source heat (SGSH) utilization. A previously developed

thermo-hydraulic model [24–26], to study heat and moisture transport and their coupled interactions in soil, is further improved within the scope of this study. The advanced model is applied to estimate theoretical heat resources of a potential site intended to support a shallow or 5th generation heating and cooling network. To the authors' knowledge, such an advanced and on-purpose modelling tool is rare in the literature. The theoretical heat capacity is defined as the seasonal/annual heat reserve of an intact ground in response to the local climatic conditions. The model represents the soil-atmosphere interface as a surface boundary which allows complex climatic data to be incorporated in a robust manner. For example, seasonal variations of solar radiation, rainfall, humidity, air temperature, wind velocity are included in the model to predict their influence on thermal behaviour, e.g., ground heat content and temperature, and moisture behaviour, e.g., saturation level. It considers heat and moisture dissipation not only through the soil-atmosphere surface boundary but also through the surrounding soil boundaries, and therefore represents realistic field conditions. Based on the simulated temperature and saturation distributions, a transient method to estimate the capacity of SGSH is proposed. Developments of the 5th generation networks are at their early stages, and the detailed understanding of the ground behaviour in terms of its heat storage and recharge potential are of paramount importance for the success of this network [4]. This is also the focus of this paper.

The structure of this paper is as follows. Firstly, the theoretical background of the coupled model is presented. Secondly, a validation exercise is carried out to demonstrate the accuracy of the model for predicting temperature and moisture distributions of a site selected from literatures. After that, the model is applied to predict and assess the long-term ground temperature, saturation level, and heat content of a test site located in Warwickshire County, UK. Finally, a parametric sensitivity study is conducted to highlight the effects of soil types and hydraulic drainage conditions on the heat storage capacities of the ground.

## 2. Theoretical and numerical formulations

The formulations presented here are for the coupled TH behaviour of an unsaturated rigid porous soil in shallow ground, from the ground surface to around 10 m depth in Earth. The flow of heat and moisture in the rigid soil constitutes the two main processes considered in the model. The heat transport formulation is based on the conservation of energy, whereas the moisture flow is considered via mass conservation. Two primary variables, pore-water pressure  $u_l$  and temperature  $T$ , are used to formulate the governing equations. The formulated ground surface boundary considers the soil-atmosphere interface in terms of heat and moisture flows.

### 2.1. Moisture transfer

Moisture flow within unsaturated soils can be described as a two-phase process, comprising of both liquid and vapour flows. The general equation for the moisture flow can be described as:

$$\rho_l \frac{\partial(\theta_l \partial V)}{\partial t} + \frac{\partial(\rho_v \theta_a \partial V)}{\partial t} = -\rho_l \partial V \nabla \cdot \mathbf{v}_l - \rho_v \partial V \nabla \cdot \mathbf{v}_v \quad (1)$$

where  $\theta_l$  is the volumetric liquid content,  $\theta_a$  is the volumetric air content,  $\partial V$  is the incremental volume,  $t$  is the time,  $\nabla$  is the gradient operator,  $\rho_l$  is the density of the liquid water,  $\rho_v$  is the density of water vapour,  $\mathbf{v}_l$  is the velocity of the liquid water, and  $\mathbf{v}_v$  is the equivalent velocity of vapour.

The volumetric liquid and air contents  $\theta_l$  and  $\theta_a$  can be expressed in terms of the porosity  $\phi$  and the degree of saturation of pore water  $S_i$ :

$$\theta_l = \phi S_l \quad (2)$$

$$\theta_a = \phi S_a = \phi(1 - S_l) \quad (3)$$

where  $S_a$  is the degree of saturation of pore air.

The incremental volume  $\partial V$  is defined as the summation of the incremental solid volume  $\partial V_s$  and void ratio  $e$ :

$$\partial V = (1 + e)\partial V_s \tag{4}$$

Pressure head and elevation head are considered as the main mechanisms to contribute to liquid water flow, and Darcy’s law is applied:

$$\mathbf{v}_l = -K_l \left( \frac{\nabla u_l}{\gamma_l} + \nabla y \right) \tag{5}$$

where  $\gamma_l$  is the unit weight of the liquid,  $y$  is the elevation, and  $K_l$  is the unsaturated hydraulic conductivity, which is modelled using the Brooks and Corey [27] Model herein:

$$K_l = K_{ls} \left( \frac{\theta_l}{\theta_{ls}} \right)^\eta \tag{6}$$

in which  $K_{ls}$  is the saturated hydraulic conductivity,  $\theta_{ls}$  is the saturated water content, and  $\eta$  is the shape parameter.

The Van Genuchten [28] Model is used to characterize the Soil Water Characteristic Curve (SWCC) of soils, and there is:

$$\frac{\theta_l}{\theta_{ls}} = \left[ 1 + \left( \frac{h}{h_g} \right)^n \right]^{-\frac{1}{n-1}} \tag{7}$$

where  $h$  is the pressure head,  $h_g$  is the scale parameter, and  $n$  is the material coefficient.

Philip and de Vries [29] proposed a vapour flow law in unsaturated soil, where the velocity of vapour is described by:

$$\mathbf{v}_v = -\frac{D_{atms} v_v \tau_v \theta_a}{\rho_l} \nabla \rho_v \tag{8}$$

in which  $D_{atms}$  is the molecular diffusivity of vapour through air,  $v_v$  is a mass flow factor,  $\tau_v$  is a tortuosity factor, and  $\nabla \rho_v$  is the spatial vapour density gradient.

The following expression proposed by Krischer and Rohnalter [30] is used to obtain the molecular diffusivity of vapour through air:

$$D_{atms} = 5.893 \times 10^{-6} \frac{T^{2.3}}{u_a} \tag{9}$$

in which  $u_a$  is the pore-air pressure that was fixed as 1atm herein.

An expression proposed by Partington [31] is adopted for the mass flow factor:

$$v_v = \frac{u_a}{u_a - u_v} \tag{10}$$

where  $u_v$  is the partial pressure of vapour, which can be calculated using the following thermodynamic relationship under assuming ‘ideal gas’ behaviour [32]:

$$u_v = \rho_v R_v T \tag{11}$$

where  $R_v$  is the specific gas constant for water vapour (461.5 J/kg/K).

A thermodynamic relationship was proposed by Edlefsen and Anderson [33], known as the psychrometric law, showing the density of water vapour can be given as:

$$\rho_v = \rho_0 \exp\left(\frac{\varphi g}{R_v T}\right) \tag{12}$$

where  $\rho_0$  is the density of saturated water vapour,  $g$  is the gravitational constant, and  $\varphi$  is the capillary potential and can be defined as:

$$\varphi = \frac{u_l - u_a}{\gamma_l} \tag{13}$$

In addition to that, the density of saturated water vapour can be obtained by the relationship proposed by Ewen and Thomas [34] as follows:

$$\rho_0 = \frac{1}{194.4 \exp(-0.06374(T - 273) + 0.1634 \times 10^{-3}(T - 273)^2)} \tag{14}$$

### 2.2. Heat transfer

The primary mechanisms of heat transfer, including conduction and convection are considered in the coupled TH model. Conservation of energy dictates the temporal derivative of the heat content  $\Omega$  is equal to the spatial derivative of the heat flux  $Q$  expressed as:

$$\frac{\partial(\Omega \partial V)}{\partial t} = -\nabla \cdot Q(\partial V) \tag{15}$$

For an unsaturated soil, its heat content per unit volume is the sum of the product of the heat storage capacity with temperature change and the contribution of enthalpy characterised by the latent heat of vaporisation [34]. There is:

$$\Omega = H_c(T - T_r) + L\phi S_a \rho_v \tag{16}$$

where  $L$  is the latent heat of vaporisation. The following equation was adopted by Ewen and Thomas [34] to calculate the heat capacity of an unsaturated soil  $H_c$  at a reference temperature  $T_r$ :

$$H_c = (1 - \phi)C_{ps}\rho_s + \phi(C_{pl}S_l\rho_l + C_{pv}S_a\rho_v) \tag{17}$$

where  $C_{ps}$ ,  $C_{pl}$ , and  $C_{pv}$  are the specific heat capacities of the solid, liquid water, and vapour, respectively, and  $\rho_s$  is the density of the solid.

Following Thomas and He [24], the heat flux  $Q$  can be defined by considering three components of heat transportation as shown below:

$$Q = -\lambda_T \nabla T + L(\mathbf{v}_v \rho_l) + (C_{pl}\mathbf{v}_l \rho_l + C_{pv}\mathbf{v}_v \rho_v)(T - T_r) \tag{18}$$

in which the first term describes the thermal conduction in accordance with Fourier’s law, the second term describes the latent heat flow associated with vapour movement, and the third term describes the heat convection in terms of the liquid phase movement and vapour phase associated with a vapour pressure gradient.

Following the approach of Thomas and Rees [25] the coefficient of thermal conductivity for an unsaturated soil  $\lambda_T$  can be defined as follows:

$$\lambda_T = \lambda_s^{\chi_s} \lambda_w^{\chi_w} \lambda_a^{\chi_a} \tag{19}$$

where  $\lambda_s$ ,  $\lambda_w$ , and  $\lambda_a$  is the thermal conductivity coefficient corresponding to the solid, water, and air component of the soil, respectively, and  $\chi_s$ ,  $\chi_w$ , and  $\chi_a$  is the volume fraction corresponding to the solid, water, and air component of the soil, respectively, which can be presented by the following expressions:

$$\chi_s = 1 - \phi \tag{20}$$

$$\chi_w = \phi S_l \tag{21}$$

$$\chi_a = \phi(1 - S_l) \tag{22}$$

### 2.3. Ground surface boundary

#### 2.3.1. Heat flow at the soil-atmosphere interface

In the coupled TH model, four major mechanisms of heat exchange between the ground surface and atmosphere are considered, that is, shortwave heat radiation, longwave heat radiation, sensible heat radiation, and latent heat radiation. The effects of organisms, such as vegetation, are not considered. Therefore, the energy balance equation at the soil-atmosphere interface can be presented as follows [11,19,35]:

$$H = H_{SW}^{Absorbed} + (H_{LW}^{Absorbed} - H_{LW}^{Emitted}) - H_{SEN} - H_{LE} \quad (23)$$

in which  $H$  is the total heat radiation flux absorbed or emitted at the soil surface,  $H_{SW}^{Absorbed}$  is the absorbed shortwave radiation flux,  $H_{LW}^{Absorbed}$  is the longwave radiation flux absorbed at the ground surface,  $H_{LW}^{Emitted}$  is the longwave radiation flux emitted at the ground surface,  $H_{SEN}$  is the sensible heat radiation flux, and  $H_{LE}$  the latent heat radiation flux.

The absorbed shortwave radiation flux can be expressed as follows [36]:

$$H_{SW}^{Absorbed} = (1 - \epsilon_{SW})H_{SW} \quad (24)$$

where  $\epsilon_{SW}$  is the shortwave reflection factor associated with the ground surface type, and  $H_{SW}$  is the shortwave radiation flux striking the ground surface (shortwave solar radiation).

The longwave radiation flux absorbed at the ground surface from the atmosphere is given as [37,38]:

$$H_{LW}^{Absorbed} = \epsilon_{LW}^A \cdot \sigma \cdot (1 + 0.17C_{cloud}^2) \cdot (T_{air})^4 \quad (25)$$

where  $\sigma$  is the Stefan-Boltzmann constant ( $5.67 \times 10^{-8} \text{ W/m}^2/\text{K}^4$ ),  $C_{cloud}$  is the fractional cloud cover coefficient (0 for clear sky and 1 for totally overcast),  $T_{air}$  is the absolute temperature of the air adjacent to the ground surface (ambient air temperature), and  $\epsilon_{LW}^A$  is the long-wave emissivity of the air at ground level (non-dimensional) which can be obtained by:

$$\epsilon_{LW}^A = 9.2 \times 10^{-6} \cdot T_{air}^2 \quad (26)$$

The longwave radiation flux emitted at the ground surface can be calculated by the Stefan-Boltzmann's law [39]:

$$H_{LW}^{Emitted} = \epsilon_{LW} \cdot \sigma \cdot T^4 \quad (27)$$

where  $\epsilon_{LW}$  is the long-wave emissivity of the ground (non-dimensional).

The sensible heat radiation flux is given as the following equation [36]:

$$H_{SEN} = \rho_a \cdot C_{pa} \cdot (T - T_{air}) \cdot C_y \cdot u_y \quad (28)$$

where  $\rho_a$  is the air density,  $C_{pa}$  is the specific heat capacity of air,  $u_y$  is the wind speed at an elevation  $y$  (wind speed), and  $C_y$  is a drag coefficient (non-dimensional).

The latent heat flux due to evaporation is calculated as follows [36]:

$$H_{LE} = LE \quad (29)$$

where  $L$  is the latent heat of vaporisation, and  $E$  is the evaporation flux (saturated state), and it can be obtained by the following equation [36, 40]:

$$E = \rho_a \cdot (q - q_{air}) \cdot C_y \cdot u_y \quad (30)$$

in which  $q$  is the specific humidity of the soil at the ground surface, and  $q_{air}$  is the specific humidity of air.

The value obtained by Equation (30) is equal to the so-called potential evaporation which can be described as the upper limit or the maximum rate of evaporation from a surface when it is saturated [41]. As the upper surface of soil would enter the unsaturated state, the following modification is made to  $E$  and there is [42]:

$$E_a = E \left( \frac{h_{ground} - h_{air}}{1 - h_{air}} \right) \quad (31)$$

where  $E_a$  is the actual evaporation flux (unsaturated state),  $h_{ground}$  is the relative humidity of the ground surface, and  $h_{air}$  the relative humidity of air at the ground surface (air relative humidity).

### 2.3.2. Moisture flow at the soil-atmosphere interface

Assuming the net moisture flux at the surface is a function of hydrological process only, the ground moisture flux can be presented as

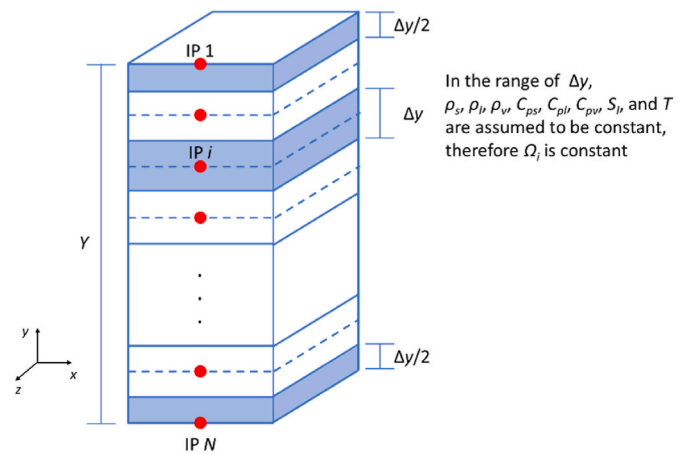


Fig. 1. Schematic showing  $N$  inspected points along the domain depth.

follows [35,43]:

$$Q_m = P - E_a - R \quad (32)$$

where  $Q_m$  is the net moisture mass flux at the ground surface,  $P$  is the precipitation mass flux (rainfall), and  $R$  is the run-off.

Therefore, based on Equations 23–32, there are five climatic variables needed in the coupled TH model to model the ground surface boundary in terms of heat and moisture exchanges between the ground surface and the atmosphere, including ambient air temperature  $T_{air}$ , shortwave solar radiation  $H_{SW}$ , air relative humidity  $h_{air}$ , wind speed  $u_y$ , and rainfall  $P$ .

### 2.4. Numerical formulation

The coupled TH model presented in this paper has been developed within the framework of a bespoke thermo-hydraulic-chemical-mechanical (THCM) modelling code, namely, COMPASS (COde of Modelling PARTially Saturated Soils) [24].

In the model, the governing transport equations are expressed in terms of the primary variables, i.e., pore-water pressure  $u_l$  and temperature  $T$ . Equation (1) and Equation (15) can be expressed as follows:

$$C_{ll} \frac{\partial u_l}{\partial t} + C_{lr} \frac{\partial T}{\partial t} = \nabla \cdot [K_{ll} \nabla u_l] + \nabla \cdot [K_{lr} \nabla T] + J_l \quad (33)$$

$$C_{TT} \frac{\partial T}{\partial t} + C_{Tl} \frac{\partial u_l}{\partial t} = \nabla \cdot [K_{TT} \nabla T] + \nabla \cdot [K_{Tl} \nabla u_l] + J_T \quad (34)$$

The  $C$  and  $K$  terms represent storage and flux, respectively, and detailed in the Supplementary Information (SI). Within the framework of COMPASS, the Galerkin finite-element method [44] is adopted to spatially discretize the model equations, e.g., Equations (33) and (34), and an implicit mid-interval backward difference time-stepping algorithm is employed for temporal discretisation. The discretized system of linear equations is solved iteratively using a predictor-corrector algorithm [45]. Furthermore, regarding the ground surface boundary, which is prescribed by two fluxes, one representing thermal interactions and the other representing hydraulic surface interactions, a sequential algorithm was developed and implemented within COMPASS code [26].

### 2.5. Heat content and heat storage of shallow ground

As presented earlier, the heat content for an unsaturated soil per unit volume  $\Omega$  ( $\text{J/m}^3$ ) in Equation (15) denotes the intrinsic energy for the ground in a certain status:

$$\Omega = [(1 - \phi)C_{ps}\rho_s + \phi(C_{pl}S_l\rho_l + C_{pv}S_a\rho_v)](T - T_r) + L\phi S_a\rho_v \quad (35)$$

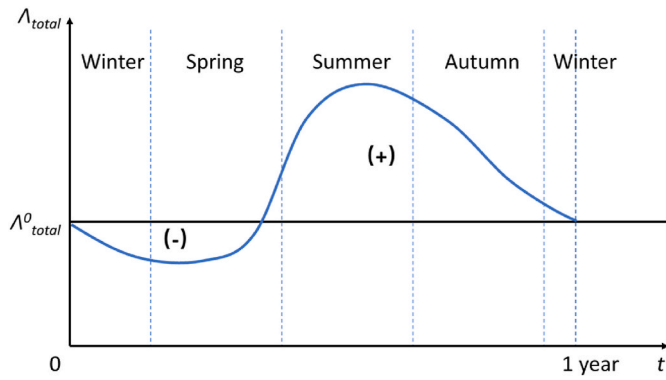


Fig. 2. Schematic showing the total heat content per unit area for the whole domain varies with time (not scaled, (+) means heat accumulation, and (-) means heat loss).

Assuming the ground consists of multi-layers of soils whose heat content can be distinct but only varies along with the depth, the layer-wise summation method is used to approximately calculate the total heat content per unit area for the ground, which is denoted by  $\Lambda_{total}$  ( $J/m^2$ ).

As shown in Fig. 1, there are  $N$  inspected points (IP) evenly taken along the domain depth. For the  $i$ th inspected point, it is assumed that the soil's density, specific heat capacity, saturation, and temperature are constant, namely, the heat content per unit volume  $\Omega_i$  ( $J/m^3$ ) is constant based on Equation (35) in the thickness of  $\Delta y$  (m) (for IP 1 on the top of the domain and IP  $N$  on the bottom of the domain, the corresponding thickness is  $\Delta y/2$ ). Therefore, the total heat content per unit area  $\Lambda_{total}$  ( $J/m^2$ ) for the whole domain can be estimated by the following equation:

$$\Lambda_{total} = \Omega_1 \frac{\Delta y}{2} + \sum_{i=2}^{N-1} \Omega_i \Delta y + \Omega_N \frac{\Delta y}{2} \quad (36)$$

where:

$$\Delta y = \frac{Y}{N - 1} \quad (37)$$

in which  $Y$  is the total depth of the ground domain (m). It should be noted that when the number of inspected points is great enough, the calculated total heat content per unit area  $\Lambda_{total}$  can be close to the actual value of the ground. A similar method can be adopted to assess the total heat content per unit area for each soil layer.

Under the influences of the varied climatic conditions, the total heat content per unit area for the whole domain changes with time, which can be hypothetically illustrated by Fig. 2. In a calendar year with four seasons, the value of  $\Lambda_{total}$  would decrease with the decline of temperature and solar radiation in Autumn and Winter, while increase with the rise of temperature and solar radiation in Spring and Summer. Correspondingly, in contrast to the starting time  $t = 0$  in a year with the initial total heat content per unit area  $\Lambda_{total}^0$ , a +ve value of  $\Lambda_{total}$  in Summer and Autumn means heat accumulation, while a -ve value of  $\Lambda_{total}$  indicates heat is loss in the rest of the year.

Due to heat being accumulated and lost in a year, the annual net heat content per unit area  $N_{HC}$  ( $J/m^2$ ) for the whole domain can also be estimated by the summation method as follows:

$$N_{HC} = \sum_{j=1}^M (\Lambda_{total}^j - \Lambda_{total}^0) \quad (38)$$

in which  $M$  is the number of  $\Lambda_{total}^j$  in a year and  $M = 365$ , and  $\Lambda_{total}^j$  is the heat content per unit area for the whole domain in the  $j$ th day ( $J/m^2$ ). A similar method can be employed to obtain the annual net heat content for each soil layer and seasonal/monthly net heat content per

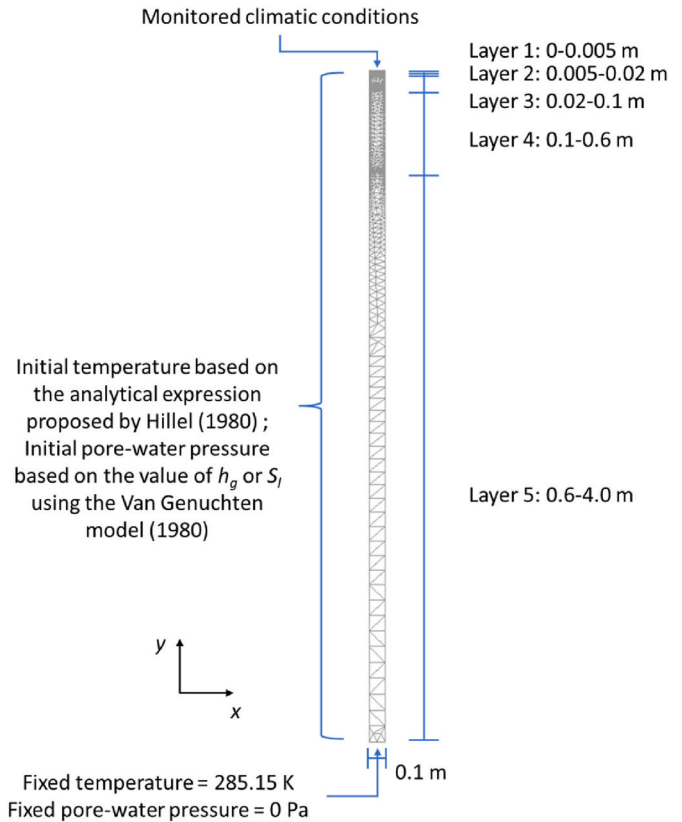


Fig. 3. Schematic showing the initial and boundary conditions and discretized mesh used in the validation.

unit area for the whole domain and each soil layer.

Assuming the area of the ground model domain is known as  $A$  ( $m^2$ ), then the annual net heat storage  $N_{HS}$  (J) for the ground domain can be obtained as follows:

$$N_{HS} = N_{HC} \times A \quad (39)$$

### 3. Model validation

Based on the literature review and sourced data, the validation of the coupled TH model with the ground surface boundary was carried out by comparing the simulated evaporation at the soil atmospheric interface against the measurements of an in-situ experimental study conducted in Southern France by Enrique et al. [46] and Calvet et al. [47]. Sensors were installed to monitor the surface water exchanges and the soil investigation was conducted to measure the soil properties at the site. The thermal and hydraulic behaviour of the ground at the site throughout the monitoring period (1 January 1995 to 7 March 1995) was simulated.

#### 3.1. Initial and boundary conditions

A 2D simulation was carried out for validation. As shown in Fig. 3, the model domain has a depth of 4 m and a width of 0.1 m, and it is made up of five layers. The selected domain was discretized into 5718 triangular elements connected by 3091 nodes. Finer mesh size was set near the ground surface than the rest of the domain.

The soil at the site has been described as a typical hydromorphic 'boulbène' with a silt loam texture for the 1 m depth surface layer (14% sand and 28% clay). However, the clay fraction increased from 17% at the surface to 40% at 1 m depth. As shown in Fig. 3, five layers of soils were determined for the first 1.3 m by Enrique et al. [46] and Calvet et al. [47].

**Table 1**  
Parameters to determine the initial ground temperature [26,48].

Parameter	$T_a$ (°C)	$A_0$ (°C)	$t_0$ (d)	$D_h$ (m <sup>2</sup> /d)
Value	10	3.333	14	0.01416

**Table 2**  
Simulation scenarios.

Number	$u_{i0}^*$ (Pa)
Base case	Determined based on the value of $h_g$ in Table 3
Case 1	Determined based on $S_i = 0.75$ using the Van Genuchten [28] Model
Case 2	Determined based on the residual saturation using the Van Genuchten [28] Model

Note: \* - initial pore-water pressure.

**Table 3**  
Material parameters for the five soil layers [46,47].

Layer	$ y $ (m)	$\phi$ (-)	$\theta_{ls}$ (-)	$h_g$ (m)	$n$ (-)	$K_{ls}$ (m/s)	$\eta$ (-)
1	0–0.005	0.48	0.48	–1.62	2.30	4.80E-6	9.30
2	0.005–0.2	0.46	0.46	–1.62	2.30	9.80E-6	9.30
3	0.2–0.1	0.40	0.40	–1.62	2.30	5.00E-7	9.30
4	0.1–0.6	0.35	0.35	–1.70	2.27	7.50E-8	10.60
5	0.6–4.0	0.30	0.30	–2.00	2.13	1.00E-10	33.30

In the simulation, the initial ground temperature was approximated using an analytical expression proposed by Hillel [48], which provides the ground temperature profile based on soil parameters and climatic conditions, given as:

$$T(y, t) = T_a + A_0 \exp\left(-\frac{y}{d}\right) \sin\left[\frac{2\pi(t - t_0)}{365} - \frac{y}{d} - \frac{\pi}{2}\right] \quad (40)$$

where  $T(y, t)$  is the soil temperature at time  $t$  (d) and depth  $y$  beneath the ground surface (m),  $T_a$  is the constant ground temperature (°C),  $A_0$  is the annual amplitude of the surface soil temperature (°C),  $t_0$  is the lag time from arbitrary start date to the occurrence of the minimum soil temperature in a year (d), and  $d$  is a damping depth, which is calculated as:

$$d = \sqrt{\frac{2D_h}{\omega}} \quad (41)$$

where  $D_h$  is thermal diffusivity (m<sup>2</sup>/d), and  $\omega$  is  $2\pi/365$  (d<sup>-1</sup>).

The parameters to determine the initial ground temperature are listed in Table 1. Although the ground temperature of the site in Southern France is not available in the literature [46,47], according to the on-site measurement elsewhere and literature data [26,49], the seasonal fluctuations in ground temperature decrease with the increasing depth. In addition, the lower the latitude, the higher the ground temperature at the same depth. Taking the UK as an example, mean annual temperatures at 1 m depth ranged from 12.7 °C in southern England to 8.8 °C in northern Scotland [49]. At the Wallingford weather station in the UK, a mean undisturbed ground temperature at 4 m beneath the ground surface was about 12 °C, with slight seasonal fluctuations [49]. Therefore, a fixed temperature with the reasonable value of 12 °C (285.15 K) was prescribed to the bottom of the domain for the current case.

Due to the lack of information on the initial pore-water pressure in the literature [46,47], several scenarios, as shown in Table 2, are made

**Table 4**  
Soil and surface boundary-related parameters [19,20,26,47,50].

Parameter	$\rho_s$ (kg/m <sup>3</sup> )	$C_{ps}$ (J/kg/K)	$\lambda_s$ (W/m/K)	$\rho_l$ (kg/m <sup>3</sup> )	$C_{pl}$ (J/kg/K)	$\lambda_w$ (W/m/K)	$C_{pw}$ (J/kg/K)	$L$ (J/kg)
Value	2700.00	736.90	2.93	1000.00	4180.00	0.57	1870.00	2260.00E3
Parameter	$\rho_a$ (kg/m <sup>3</sup> )	$C_{pa}$ (J/kg/K)	$\lambda_a$ (W/m/K)	$T_r$ (K)	$\epsilon_{SW}$ (-)	$C_{cloud}$ (-)	$\epsilon_{LW}$ (-)	$C_y$ (-)
Value	1.225	1000.00	0.025	273.15	0.215	0.770	0.960	0.004

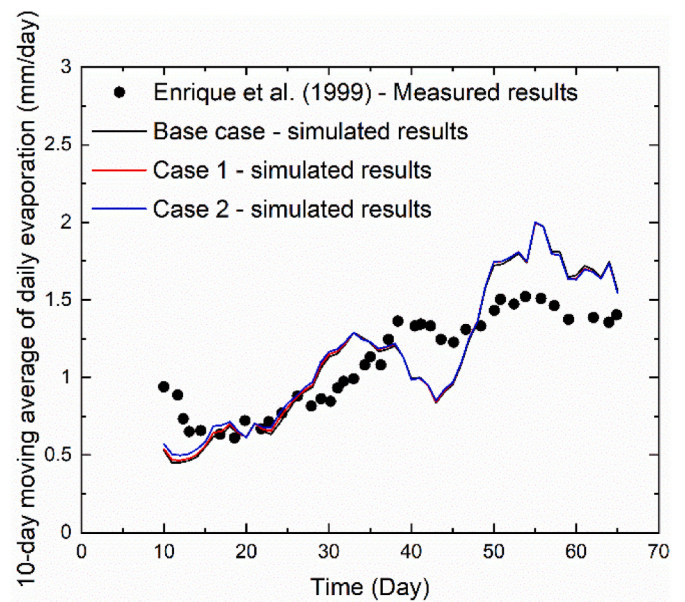


**Fig. 4.** Daily evaporation as measured and simulated using a 10-day moving average (after [46]).

to calculate the initial pore-water pressure based on the value of  $h_g$  and  $S_i$  using the Van Genuchten [27] Model. Moreover, a water table was reported to be at a depth of 4 m below the ground surface during the inspection period [46], and therefore, the pore-water pressure was fixed as 0 Pa at the bottom of the domain.

The climatic variables of ambient air temperature, shortwave solar radiation, wind speed, air relative humidity, and rainfall were prescribed uniformly on the top of the domain (ground surface), and their variations can refer to Enrique et al. [46].

### 3.2. Material parameters

Each layer of soil was assumed to be isotropic in the simulation. The soil properties involving the hydraulic conductivity and SWCC have been summarized in Table 3 based on the measurements conducted by Enrique et al. [46] and Calvet et al. [47]. It should be mentioned that there were no material data available beyond the depth of 1.3 m, hence the material parameter for soils from the depth of 1.3 m–4.0 m was assumed to be the same as the fifth layer of soil. In addition, other soil parameters, such as the solid’s density, specific heat capacity and thermal conductivity, as well as surface boundary-related parameters were gathered from the literature, as listed in Table 4.

### 3.3. Validation results

As shown in Table 2, three scenarios were adopted to determine the initial pore-water pressure for each layer of soil. The simulated daily evaporation and the measured data collected at the monitoring site are compared in Fig. 4.

From the figure, it can be seen that the maximum absolute error between the Base case and the measurement was 0.5 mm/day for the 65-day simulation period. Although there are variations between the simulated Base case results and the measured data, which may be caused



Fig. 5. Test site at the University of Warwick and borehole logs obtained from BGS [51].

by the initial conditions assumed and the material parameters used, the modelling presented herein can capture the changing pattern of the daily evaporation. Furthermore, the daily evaporation simulated by the Base case, Case 1, and Case 2 shows no significant differences. Therefore, the daily evaporation calculation is not sensitive to the assumption of the initial pore-water pressure in the soils.

Based on the aforementioned validation, it can be concluded that the surface ground boundary considering a range of climatic variables and mechanisms has been correctly implemented in the coupled TH model.

#### 4. Application

The coupled TH model with the ground surface boundary has been applied to investigate the long-term (5 years) ground behaviour in the campus of the University of Warwick in response to seasonal climatic conditions. The findings of the test site will help to guide the utilization of the shallow ground source heat energy and the installation of the ground source heat system.

##### 4.1. Test site at Warwickshire, UK

Fig. 5 shows the test site located within the University of Warwick

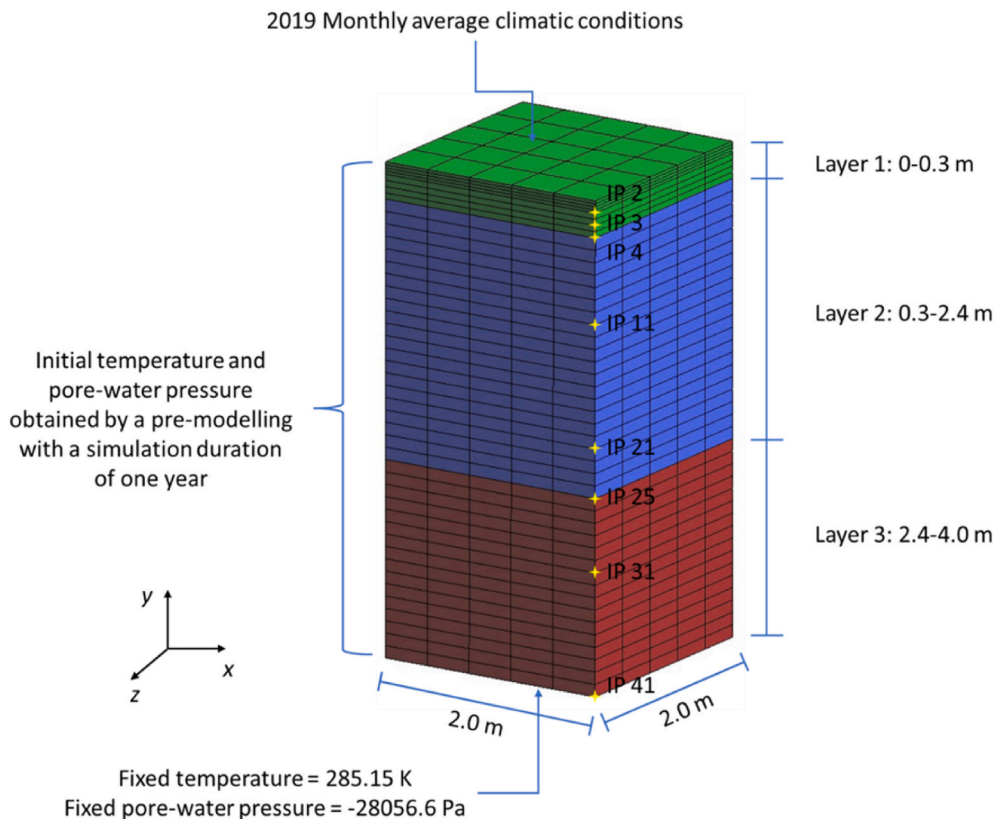


Fig. 6. Schematic showing the initial and boundary conditions and 3D discretized mesh consisted of 1125 hexahedron elements.

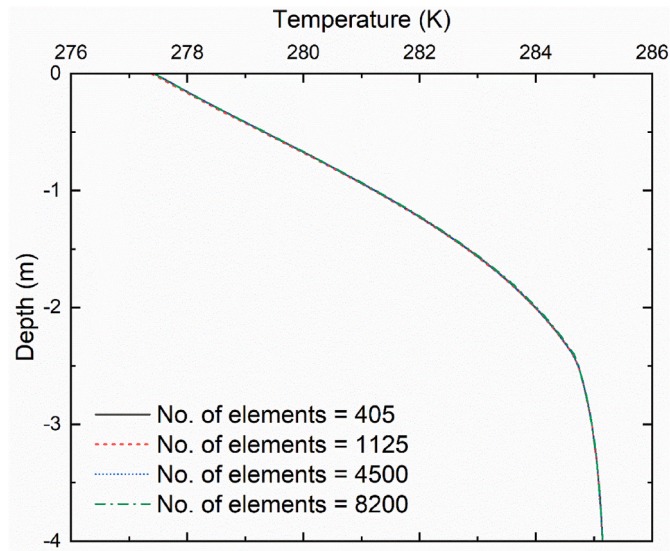


Fig. 7. Ground temperature profiles at the end of the pre-modelling exercise obtained by various mesh sizes.

campus in Warwickshire County, UK. The site is located within the case study area of the EPSRC funded “Integrated Heating and Cooling Networks with Heat-sharing-enabled Smart Prosumers” project (Grant number: EP/T022795/1). The campus is a 24/7 town of 25,000 people, with 7000 student rooms, more than 150 buildings, 3 conference centres, 2 sport centres, retails, cafes, restaurants, offices and teaching buildings, industrial and research buildings. Peak electricity and heat demand in the campus are 10 MW<sub>e</sub> and 15MW<sub>th</sub>, respectively. The heat demand in the campus is primarily met by a district heating network supplied by natural gas CHP (5 CHP units with the total capacity of 8.2 MW<sub>e</sub>) and auxiliary natural gas boilers (3 boilers with the total capacity of 14.7 MW<sub>th</sub>). The heat network is comprised of 8.87 km supply pipes and 8.87 km return pipes and operates at 100 °C supply temperature and 50 °C return temperature. The University of Warwick’s Estate Office is investigating options to decarbonise the heat system in the campus. One of the promising alternatives to the current natural gas CHP and boilers is large scale ground source heat pump.

The highlighted square with a dimension of 200 m × 200 m is the proposed test site investigated within the scope of this work. The soil profile layers are obtained from three borehole logs (as shown by red

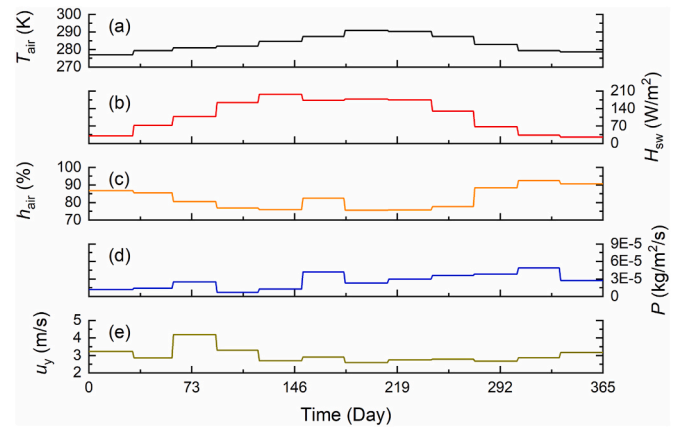


Fig. 9. Climatic variables of 2019: (a) monthly average ambient air temperature  $T_{air}$ , (b) monthly average shortwave solar radiation  $H_{SW}$ , (c) monthly average air relative humidity  $h_{air}$ , (d) monthly average rainfall  $P$ , and (e) monthly average wind speed  $u_y$ .

dots in Fig. 5) obtained from the British Geological Survey (BGS) [51] borehole database. The soil profile from the ground surface is categorized into three layers, that is, Layer 1: 0–0.3 m sandy clay loam, Layer 2: 0.3–2.4 m silty clay, and Layer 3: >2.4 m mudstone.

#### 4.2. Initial and boundary conditions

In this study, a representative unit with three soil layers was employed. It was assumed that each soil layer was uniform. In addition, a uniform ground surface was assumed owing to the intricacy of the ground surface types in the test site. The 3D domain for the representative unit is shown in Fig. 6. Based on the soil profile and the computation efficiency, the domain depth was set to 4 m, and the length and width were taken as 2 m.

A pre-modelling exercise was conducted prior to the formal 5-year simulations. The pre-modelling lasted for a year, and the initial ground temperature was approximated using the analytical expression proposed by Hillel [48], and the initial pore-water pressure for each soil layer was computed using the Van Genuchten [28] Model, assuming the initial saturation was equal to 0.75.

In order to obtain the optimal mesh, various mesh sizes were used, which was reflected by the number of elements, and the related ground

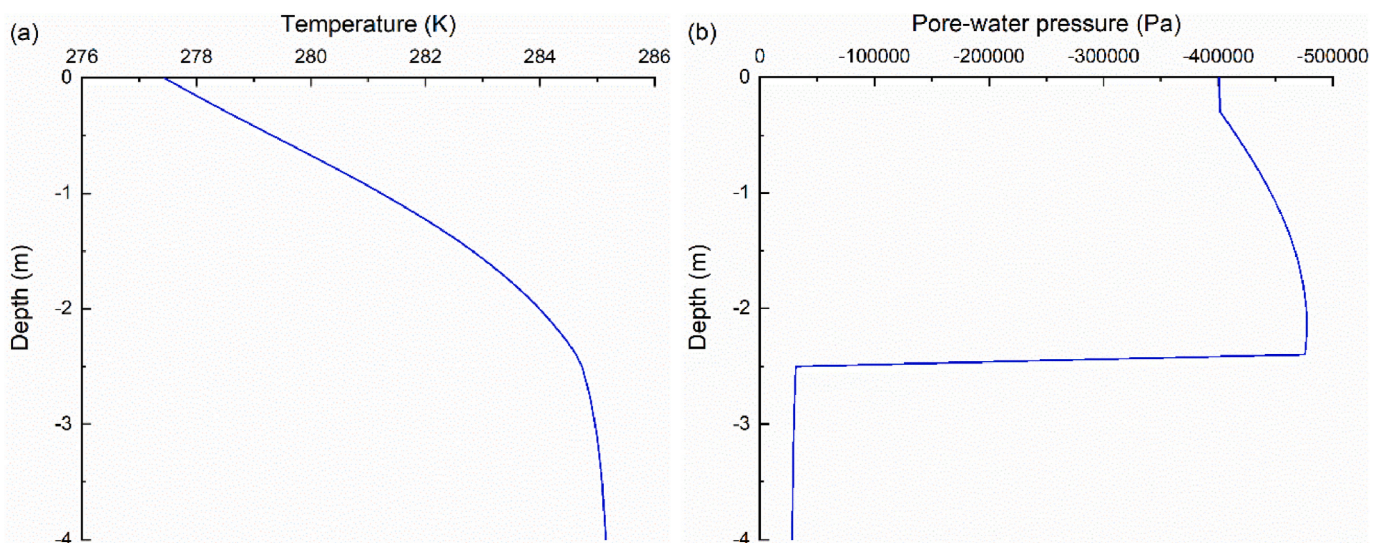


Fig. 8. Initial temperature and pore-water pressure (No. of elements = 1125) used in the long-term simulations.

**Table 5**  
Material parameters for the three soil layers [53–57].

Soil	$ y $ (m)	$\phi$ (-)	$\theta_{ls}$ (-)	$h_g$ (m)	$n$ (-)	$K_{ls}$ (m/s)	$\eta$ (-)	$\rho_s$ (kg/m <sup>3</sup> )	$C_{ps}$ (J/kg/K)	$\lambda_s$ (W/m/K)
Sandy clay loam <sup>a</sup>	0–0.3	0.51	0.51	0.123	2.095	6.400E-7	3.67	2630.0	1014.0 <sup>d</sup>	1.04 <sup>d</sup>
Silty clay <sup>b</sup>	0.3–2.4	0.60	0.60	0.471	2.223	4.051E-7	5.04	2800.0	1169.0 <sup>e</sup>	3.76 <sup>e</sup>
Mudstone <sup>c</sup>	2.4–4.0	0.51	0.51	1.020	2.268	1.882E-6	17.12	2435.0	1050.6 <sup>f</sup>	2.42 <sup>f</sup>

Note: a – Soil 4601 in the UNSODA, sandy clay loam from Cowpark, Scotland [57]; b – Soil 3120 in the UNSODA, silty clay from Canning Town, W. Bengal India; c – Weathered mudstone soil from Gyeongangbuk-do, South Korea [53]; d – Sandy clay loam from Wallingford, England [54]; e – Silty clay from Camborne, England [54]; f – Average value of ‘Sidmouth Mudstone Formation’ Mudstone [55].

**Table 6**  
Simulated cases.

Number	Layer 1 (0–0.3 m)		Layer 2 (0.3–2.4 m)	
	Soil type	$K_{ls}$ (m/s)	Soil type	$K_{ls}$ (m/s)
Base case	Sandy clay loam	6.400E-7	Silty clay	4.051E-7
Case 1	Silty clay	4.051E-7	Silty clay	4.051E-7
Case 2	Sandy clay loam	6.400E-7	Sandy clay loam	6.400E-7
Case 3	Sandy clay loam	6.400E-7	Silty clay	4.051E-4
Case 4	Sandy clay loam	6.400E-4	Silty clay	4.051E-7

temperature profiles at the end of the pre-modelling exercise were compared, as shown in Fig. 7. From the figure, it can be seen that there is a negligible difference in the ground temperature profiles as the element number of the mesh increases. Considering the computational efficiency and result accuracy, the discretized mesh consisted of 1125 hexahedron elements connected by 1656 nodes, as shown in Fig. 6, was adopted in the following simulations. Correspondingly, the ground temperature and pore-water pressure on the last day of the year became the initial ground temperature and pore-water pressure for the long-term simulations, as shown in Fig. 8.

As explained in the model validation, the mean undisturbed ground temperature at 4 m below the ground surface was about 12 °C [49], so a fixed temperature boundary (285.15 K) was prescribed at the bottom of the domain to consider the undisturbed ground temperature, and the pore-water pressure was assumed to be fixed at saturation of 0.75 at the domain bottom.

On the ground surface, climatic boundary conditions were evenly prescribed. The climatic data was obtained from a meteorological station near the University of Warwick (Church Lawford, Met Office [52]), and the most recent data of 2019 was used in the current simulations. Fig. 9 depicts the monthly average climatic variables.

4.3. Material parameters

Soil properties should ideally be measured using soil samples taken from the test site. In the current simulation, the soil properties for the three soil layers, as listed in Table 5, were derived from the literature [53–55] and the UNSODA Unsaturated Soil Hydraulic Database [56]. In addition, the values of model parameters in Table 4 were utilised and  $C_y$  was given a typical value of 0.016 [26].

4.4. Simulated scenarios

A Base case was established using the aforementioned borehole logs, material parameters, and modelling procedure. Four more cases, as listed in Table 6, are designed to study the influences of the soil types and hydraulic drainage conditions on the ground temperature and saturation, and then the heat content of ground. Different soil profiles were employed in Case 1 and Case 2 compared to the Base case. Layers 1 and 2 in Case 1 are silty clay, whereas Layers 1 and 2 in Case 2 are sandy clay loam. In contrast with the Base case, the saturated hydraulic conductivities of Layer 2 in Case 3 and Layer 1 in Case 4 were increased by 1000 times.

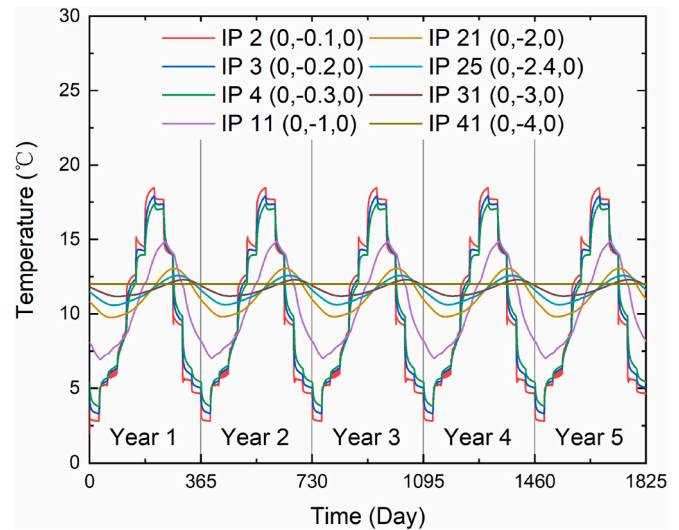


Fig. 10. Variations of temperature of selected inspected points.

5. Results

For all cases using the 3D domain consisting of 3 soil layers in Figs. 6 and 41 inspected points ( $N = 41$ ) were evenly taken along the depth, and hence the thickness of each sublayer  $\Delta y$  was 0.1 m. Among the inspected points, IPs 1–4 are in Layer 1, IPs 4–25 are in Layer 2, and IPs 25–41 are in Layer 3.

5.1. Results of base case

Upon the collective inspection of the simulated results, both the

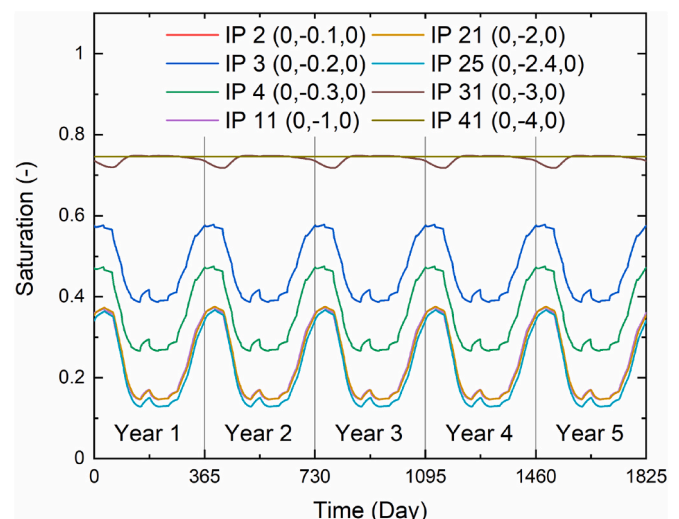


Fig. 11. Variations of saturation of selected inspected points.

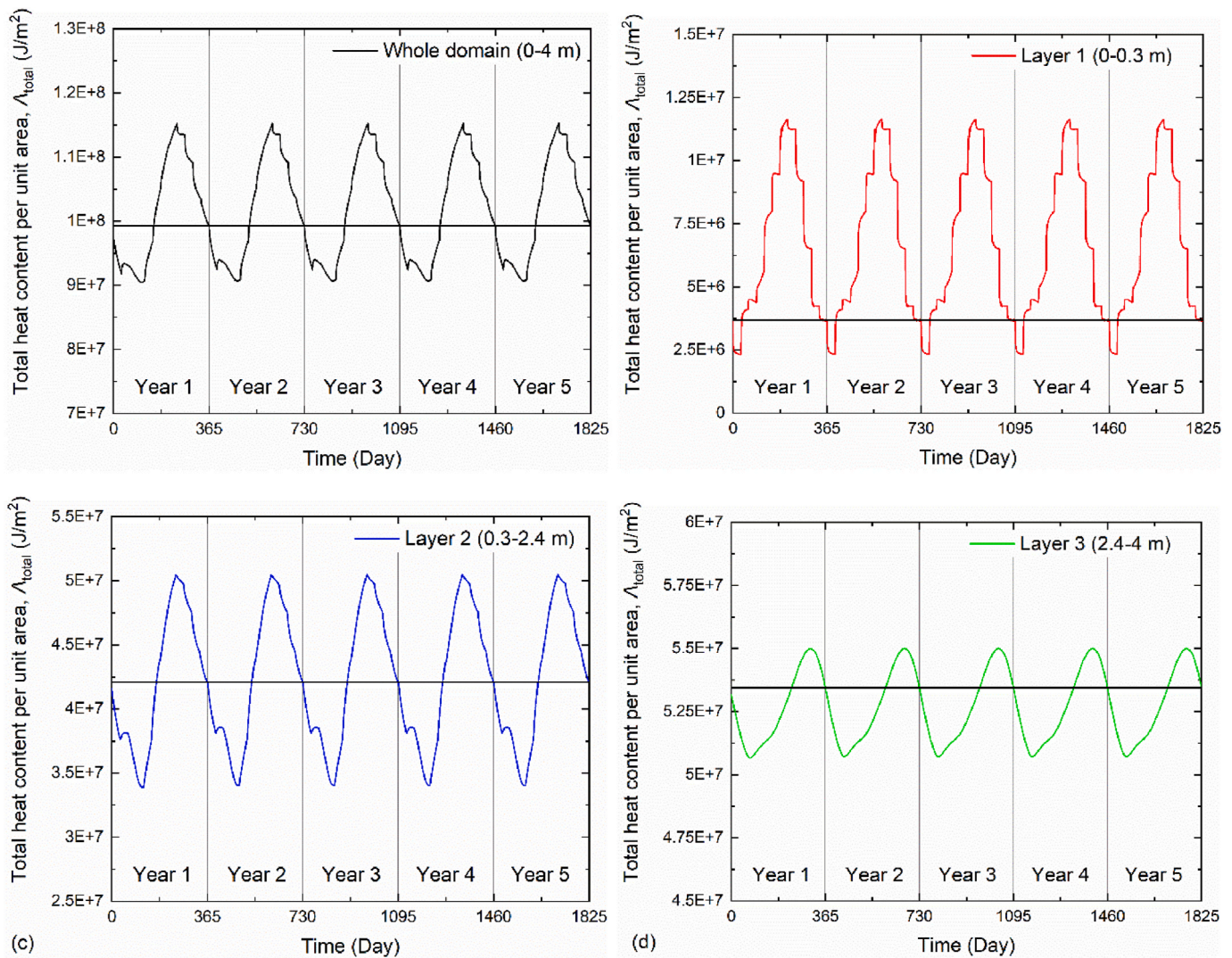


Fig. 12. Variations of total heat content per unit area for (a) the whole domain, (b) Layer 1, (c) Layer 2, and (d) Layer 3 in the Base case.

thermal and hydraulic ground behaviour reached a steady annual cycle state after approximately two years. In order to improve the clarity of plots, as shown in Fig. 6, the results of selected inspected points, including IPs 2–4, IP 11, IP 21, IP 25, IP 31, and IP41, during the 5-year simulation are illustrated. The observed cyclic behaviour was expected based upon the annually prescribed climatic data [26,58].

(1) Temperature and saturation

As demonstrated in Fig. 10, the amplitude of the simulated temperature decreased with the increase of the depth, which is consistent with previous findings [11,12,20,26]. In comparison with other inspected points, significant changes in temperature of IPs 2–4 can be easily observed, indicating that the temperature of Layer 1 was most affected by the climatic conditions. The highest and lowest temperatures of IP 2 were 291.6 K and 275.1 K, respectively, then the amplitude of IP 2 was the greatest, reaching 16.5 K. Furthermore, curve peaks were off-set one another with respect to depth, with the deeper the inspected point, the later the time, as found in the literature [11,12,20,26].

As shown in Fig. 11, the simulated saturation of IP 2 and IP 3 almost coincided, ranging between 0.58 and 0.39 annually, with the peak value occurring in mid-February and the lowest value occurring in mid-August. Insignificant differences existed in the saturation of IP 11 and IP 21, both of which were in Layer 2. At IP 25, the interface between

Layer 2 and Layer 3, the difference between the highest and lowest saturations in a year (0.37 and 0.13, respectively) was the biggest (0.24). The simulated saturation of IP 31 in Layer 3 varied slightly between 0.75 and 0.72 in a year.

(2) Heat content

The development of the total heat content per unit area for the ground  $\lambda_{total}$  with time is shown in Fig. 12. By observing the figures, values of the total heat content per unit area for the whole domain and each soil layer repeated annually after approximately 2 years.

There are four seasons in the UK and in the Western Europe: Spring is from March to May, Summer is from June to August, Autumn is from September to November, and the remaining three months are Winter. Due to the periodic dynamics as shown in Fig. 12, the results in Year 3 (Day 730 to Day 1095) were studied in great detail and illustrated in Fig. 13.

As shown in Fig. 13(a), the value of  $\lambda_{total}$  for the whole domain varied from  $9.05 \times 10^7 \text{ J/m}^2$  to  $1.15 \times 10^8 \text{ J/m}^2$ , with the maximum value on Day 973, the final day of Summer, and the lowest value on Day 826, in the middle of Spring. Compared with the initial value on Day 730 ( $9.92 \times 10^7 \text{ J/m}^2$ ), the  $\lambda_{total}$  generated from 1 January to 2 June in Year 3 (Day 730 to Day 883) was lower, indicating that the whole domain had been losing heat during this period. It was not until 3 June (Day 884) when a

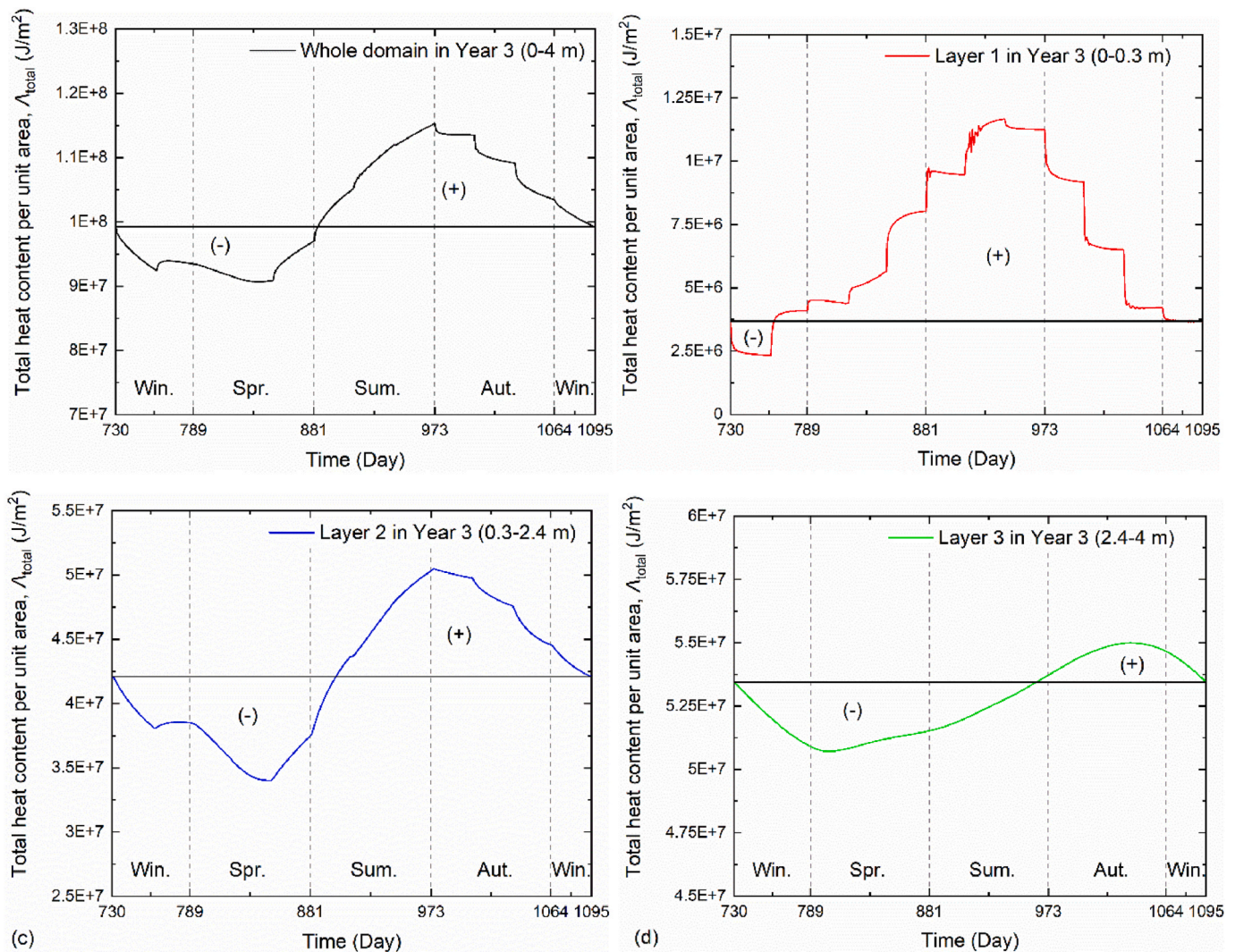


Fig. 13. Variations of total heat content per unit area for (a) the whole domain, (b) Layer 1, (c) Layer 2, and (d) Layer 3 in Year 3 of the Base case ((+) means heat accumulation, and (-) means heat loss).

higher  $\Lambda_{total}$  than the initial value on Day 730 was achieved, implying that heat was accumulated in the ground, and this trend continued until the last day of Year 3.

The total heat content per unit area for Layer 1 in Year 3 is shown in Fig. 13(b). The lowest value was  $2.32 \times 10^6 J/m^2$ , which occurred on 31 January (Day 761), and the highest value of  $\Lambda_{total}$  was  $1.16 \times 10^7 J/m^2$ , which took place on 31 July (Day 942). In comparison with the initial total heat content per unit area on Day 730 which was  $3.69 \times 10^6 J/m^2$ , a lower value of  $\Lambda_{total}$  was only produced in the first 33 days in Year 3 (primarily in January), which indicated that Layer 1 was storing heat for about 91% of the year, mainly in Spring, Summer, and Autumn.

Fig. 13(c) presents the total heat content per unit area for Layer 2 in Year 3. As can be seen from the figure, the highest and the lowest value of  $\Lambda_{total}$  were  $5.05 \times 10^7 J/m^2$  and  $3.40 \times 10^7 J/m^2$ , respectively, on 2 September and 1 May (Day 975 and Day 851), respectively. In the first 170 days of Year 3, a smaller  $\Lambda_{total}$  than the initial value on Day 730 ( $4.20 \times 10^7 J/m^2$ ) was produced, implying that Layer 2 had been losing heat for almost half of the year.

The total heat content per unit area for Layer 3 in Year 3 is given in Fig. 13(d). The value of  $\Lambda_{total}$  in this layer changed from  $5.07 \times 10^7 J/m^2$  to  $5.5 \times 10^7 J/m^2$ . In Year 3, Layer 3 kept losing heat until 22 August (Day 964) when a higher  $\Lambda_{total}$  than the initial value on Day 730 ( $5.34 \times 10^7 J/m^2$ ) was generated, which indicated that heat began to accumulate for the remaining time.

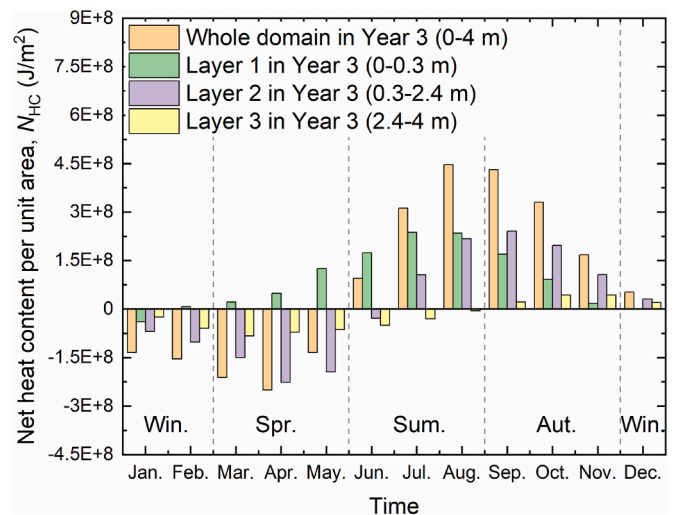


Fig. 14. Seasonal and monthly net heat content per unit area in Year 3 of the Base case.

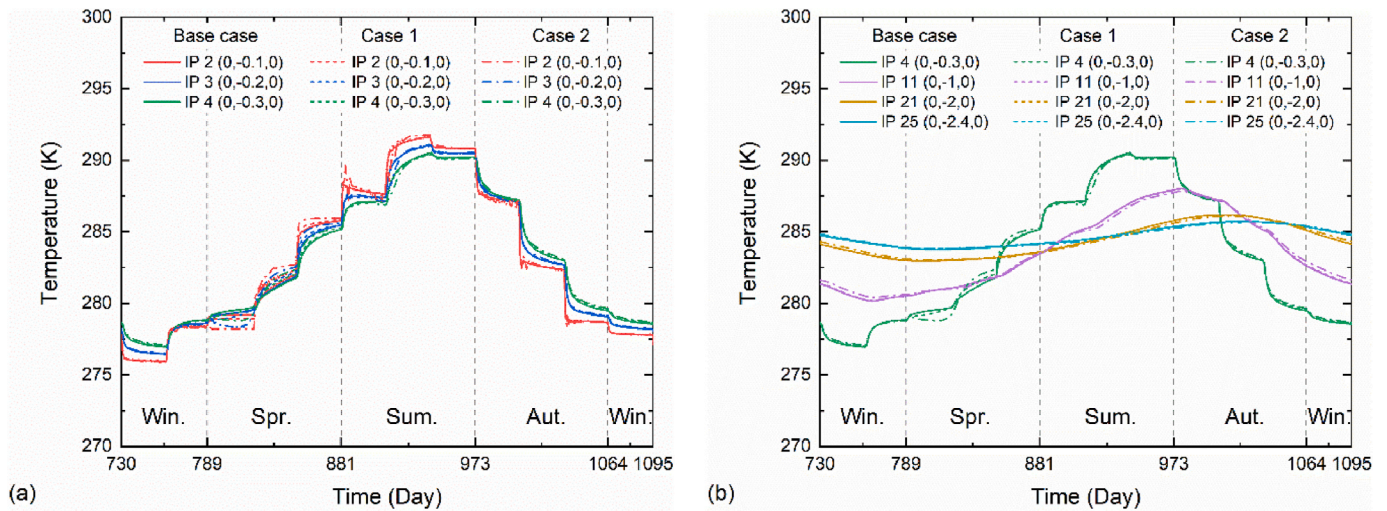


Fig. 15. Variations of temperature of inspected points in (a) Layer 1 and (b) Layer 2 of the Base Case, Case 1, and Case 2.

On the basis of the total heat content per unit area in Year 3 (Fig. 13) and Equation (38), the annual net heat content per unit area  $N_{HC}$  for the whole domain and each soil layer can be calculated and summarized in Table A1 of the SI. The annual net heat content per unit area for the whole domain was positive and reached  $9.52 \times 10^8 \text{ J/m}^2$ , which indicated that complementary heat derived from solar radiation was stored in the ground. The 0.3 m-thick Layer 1 contributed the most, which was as high as  $1.09 \times 10^9 \text{ J/m}^2$ , while the 2.1 m-thick Layer 2 only provided  $1.26 \times 10^8 \text{ J/m}^2$ . Compared with  $N_{HC} > 0$  for Layers 1 and 2, the value of  $N_{HC}$  for Layer 3 was negative with a value of  $-2.61 \times 10^8 \text{ J/m}^2$ , showing that heat was lost via Layer 3 during the year.

The seasonal and monthly net heat content per unit area  $N_{HC}$  for the whole domain and each soil layer were computed and provided in Table A1 of the SI using a similar method. Fig. 14 illustrated changes in the seasonal and monthly net heat content per unit area for the whole domain and each soil layer.

According to the data and figure, for the whole domain,  $N_{HC} > 0$  can be obtained in Summer and Autumn. The value of  $N_{HC}$  in Summer was  $9.30 \times 10^8 \text{ J/m}^2$ , which was very close to the annual net value ( $9.52 \times 10^8 \text{ J/m}^2$ ), and most of it came from August with the value of  $4.47 \times 10^8 \text{ J/m}^2$ .

For Layer 1,  $N_{HC} > 0$  can be produced in Spring, Summer, and Autumn, and the value of  $N_{HC}$  in Summer was the largest, reaching  $6.45 \times 10^8 \text{ J/m}^2$ , which accounted for 59.2% of the whole year ( $1.09 \times 10^9 \text{ J/m}^2$ ).

Among the twelve months, the value of  $N_{HC}$  in July was the highest and it was  $2.37 \times 10^8 \text{ J/m}^2$ . It should be noted that the current simulation's monthly  $N_{HC}$  for Layer 1 was consistent with heat flux values for shallow depth soil in the literature [11,12,16,59].

For Layer 2, it can be observed from the table and figure that  $N_{HC} > 0$  took place in Summer and Autumn, and Autumn had a larger positive  $N_{HC}$  equalled to  $5.44 \times 10^8 \text{ J/m}^2$ , much higher than the annual value of  $1.26 \times 10^8 \text{ J/m}^2$ . Throughout the year,  $N_{HC}$  in September was the highest, reaching  $2.40 \times 10^8 \text{ J/m}^2$ .

Although the annual value of  $N_{HC}$  was negative for Layer 3,  $N_{HC} > 0$  can still be found in Autumn with a value of  $1.08 \times 10^8 \text{ J/m}^2$ . The value of  $N_{HC}$  in November was the greatest in the year and it was  $4.32 \times 10^7 \text{ J/m}^2$ .

Based on the net heat content per unit area listed in Table A1 of the SI and considering the  $200 \text{ m} \times 200 \text{ m}$  inspected site in the University of Warwick, the annual/seasonal/monthly net heat storage  $N_{HS}$  for the whole domain and each soil layer can be estimated following Equation (39). A large amount of heat from the solar radiation can be stored in the ground. For instance, the annual net heat storage for the whole domain reached  $3.81 \times 10^{13} \text{ J}$ , which can be potentially used as shallow ground source heat for building heating as environment-friendly energy. Among which, the annual net heat storage for Layer 1, Layer 2, and Layer 3 was  $4.35 \times 10^{13} \text{ J}$ ,  $5.06 \times 10^{12} \text{ J}$ , and  $-1.04 \times 10^{13} \text{ J}$ , respectively.

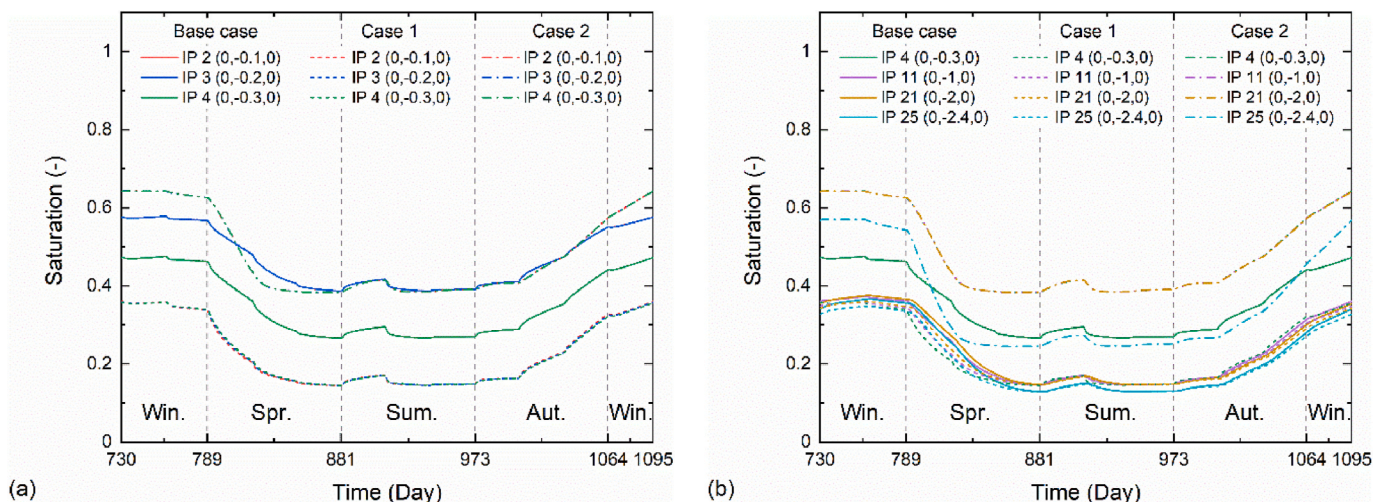


Fig. 16. Variations of saturation of inspected points in (a) Layer 1 and (b) Layer 2 of the Base case, Case 1, and Case 2.

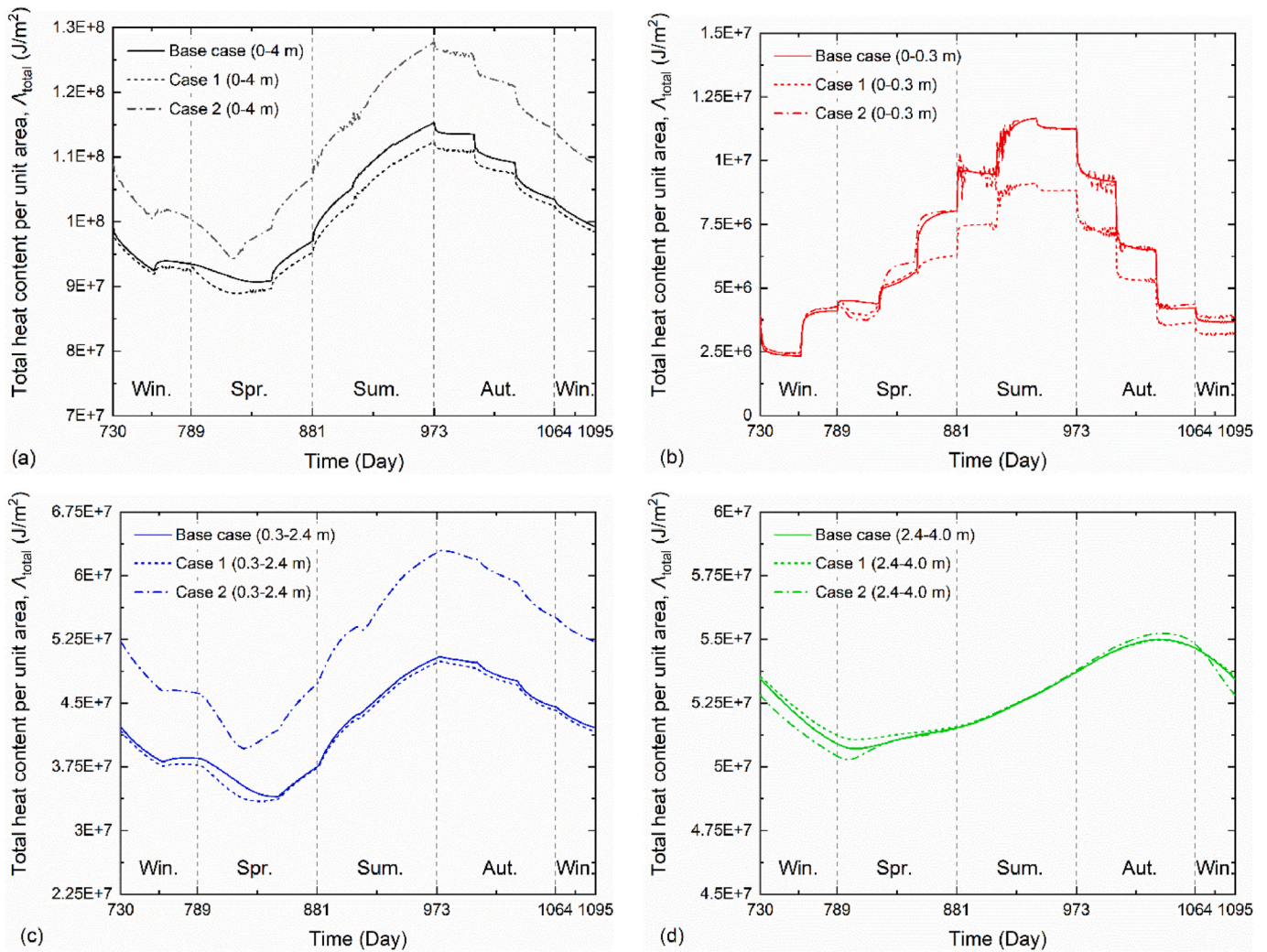


Fig. 17. Variations of total heat content per unit area for (a) the whole domain, (b) Layer 1, (c) Layer 2, and (d) Layer 3 in Year 3 of the Base case, Case 1, and Case 2.

5.2. Influence of soil types – result comparison of base case, case 1, and case 2

The ability of the soil layer to store and conduct heat is related to the type of soil [11,16,18]. In addition to the soil profile in the Base case, Case 1 and Case 2 with different soil profiles were carried out (see Table 6), and their results were compared.

(1) Temperature and saturation

Variations of the temperature of inspected points in Year 3 of the Base case, Case 1, and Case 2 are illustrated in Fig. 15. Although various soil profiles were adopted in the Base case, Case 1, and Case 2, the temperature changes for Ips in Layer 1 and Layer 2 were not significantly different, as shown in Fig. 15(a) and (b), respectively.

Fig. 16(a) and Fig. 16(b) depict the saturation variations for inspected points in Layer 1 and Layer 2, respectively. The variations in soil types are reflected in the disparities in Ips’ saturation. Saturation was lower for Ips in Layers 1 and 2 in Case 1 than that for Ips at the same depth in the Base case. In contrast with the Base case, there was a generally higher saturation for Ips in Layer 1 in Case 2, especially during Winter. Meanwhile, Case 2 exhibited greater saturation than the Base case for Ips at the same depth in Layer 2.

(2) Heat content

Fig. 17 shows the total heat content per unit area for the whole domain and each soil layer obtained by the Base case, Case 1, and Case 2 in Year 3. According to Fig. 17(a), which presents the value of  $\Lambda_{total}$  for the whole domain, the development trends of  $\Lambda_{total}$  in the three cases were comparable, while from the perspective of the value of  $\Lambda_{total}$  for the whole domain, Case 2 > Base case > Case 1, as a result of the differences in  $\Lambda_{total}$  for each soil layer. Inspecting the variations of  $\Lambda_{total}$  for Layer 1, Layer 2, and Layer 3, as shown in Fig. 17(b), (c), and Fig. 17(d), respectively, it can be found that: (1) the values of  $\Lambda_{total}$  for Layer 1 in the Base case and Case 2 were close, and both were higher than that in Case 1; (2) the values of  $\Lambda_{total}$  for Layer 2 in the Base case and Case 1 were similar, and both were much lower than that in Case 2; and (3) there were small differences in the values of  $\Lambda_{total}$  for Layer 3 in the three cases. The initial value, maximum value, and minimum value of the total heat content per unit area in Year 3 of the Base case, Case 1, and Case 2 are compared in Fig. 18.

The values of the monthly net heat content per unit area  $N_{HC}$  in Year 3 of the Base case, Case 1, and Case 2 are compared in Fig. 19. The values of the net heat content per unit area in Year 3 of Case 1 and Case 2 are provided in Table A2 and Table A3 of the SI, respectively. For the whole domain (0–4 m), among the three cases, Case 2 exhibited the lowest monthly  $N_{HC} < 0$  (in March), but also the highest positive monthly  $N_{HC} > 0$  (in August). For Layer 1 (0–0.3 m), there was insignificant difference in the monthly  $N_{HC}$  in the Base case and Case 2, and both were higher than that in Case 1. For Layer 2 (0.3–2.4 m), the variations in the

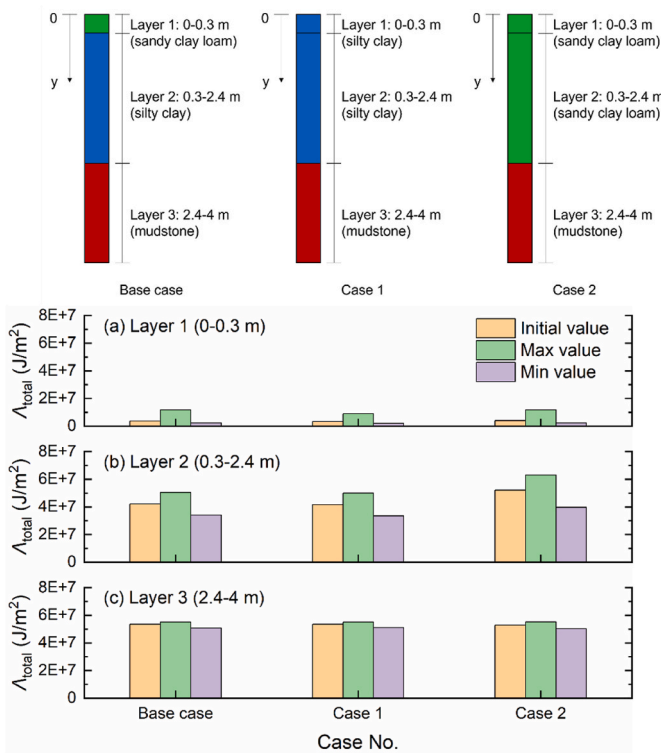


Fig. 18. Total heat content per unit area for (a) Layer 1, (b) Layer 2, and (c) Layer 3 in Year 3 of the Base case, Case 1, and Case 2.

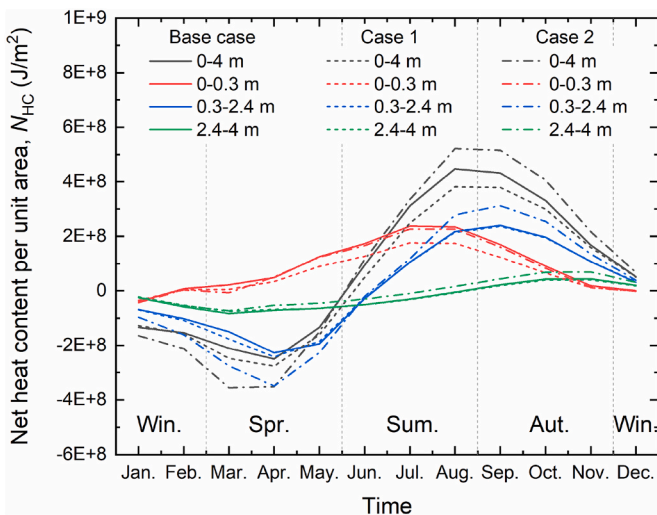


Fig. 19. Variations of monthly net heat content per unit area in Year 3 of the Base case, Case 1, and Case 2.

monthly  $N_{HC}$  in the Base case and Case 1 were comparable, while Case 2 showed the lowest monthly  $N_{HC} < 0$  in April and the highest positive monthly  $N_{HC} > 0$  in September. For Layer 3 (2.4–4 m), there were small deviations in the monthly  $N_{HC}$  in the three cases.

Superimposing the monthly net heat content per unit area shown in Fig. 19, the annual/seasonal net heat content per unit area for the whole domain and each soil layer in Case 1 and Case 2 can be obtained. Compared with the Base case, the annual  $N_{HC}$  equals to  $9.52 \times 10^8 \text{ J/m}^2$ , the values of annual  $N_{HC}$  in Case 1 and Case 2 were  $5.95 \times 10^8 \text{ J/m}^2$  and  $9.43 \times 10^8 \text{ J/m}^2$ , respectively.

Based on the aforementioned analyses, it can be concluded that the

spatial and temporal distributions of heat in soil layers of the ground can be significantly affected by the combination of the soil types (soil profile). It highlights the possibility of maximizing shallow ground source heat resources by improving soil types.

### 5.3. Influence of hydraulic drainage conditions – result comparison of base case, case 3, and case 4

The saturated hydraulic conductivity of the soil would affect the drainage conditions in the ground. Higher hydraulic conductivity results into faster drainage and vice versa. Using the same model parameters as in the Base case but specifying a higher saturated hydraulic conductivity for Layer 2 in Case 3 and Layer 1 in Case 4 (see Table 6), the results of the Base case, Case 3, and Case 4 were compared.

#### (1) Temperature and saturation

Fig. 20 shows the temperature changes of inspected points of the Base case, Case 3, and Case 4 in Year 3. As can be seen from the figure, increasing the saturated hydraulic conductivities for Layer 2 in Case 3 and Layer 1 in Case 4 by three magnitudes of orders showed negligible effect on the temperature variations in Layer 1 and Layer 2 in the three cases.

In Year 3, the saturation variations of inspected points in the Base case, Case 3, and Case 4 are illustrated in Fig. 21. It can be found that compared with the Base case, the saturation distributions in Case 3 were slightly changed, while Case 4 was basically unchanged.

#### (2) Heat content

The total heat content per unit area for the whole domain and Layers 1–3 in Year 3 of the Base case, Case 3, and Case 4 is presented by Fig. 22 (a), Fig. 22(b), (c), and Fig. 22(d), respectively. As can be seen from the figure, there were slight variations in the value of  $\Lambda_{total}$  for the three cases due to the similar temperature and saturation variations as shown in Figs. 20 and 21. The initial value, maximum value, and minimum value of the total heat content per unit area in Year 3 of the Base case, Case 3, and Case 4 are presented in Fig. A1 of the SI.

Fig. 23 compares the monthly net heat content per unit area  $N_{HC}$  in Year 3 of the Base case, Case 3, and Case 4. The values of the net heat content per unit area in Year 3 of Case 3 and Case 4 are provided in Table A4 and Table A5 of the SI, respectively. According to Fig. 23, except the monthly  $N_{HC}$  for the whole domain (0–4 m) and Layer 2 (0.3–2.4 m) in Case 3 was slightly lower than that in the Base case, insignificant differences can be found in the three cases.

Based on the above analysis, while keeping other model parameters unchanged, when the saturated hydraulic conductivity of the first and second layers increased by three orders of magnitude in the simulations, changes in the temporal and spatial distributions of the shallow ground heat were not significant.

## 6. Conclusions

In this paper, a framework to calculate and to predict theoretical heat capacity, temperature, and soil-moisture behaviour of a ground for potential exploitation of shallow ground source heat (SGSH) is presented. Atmospheric data e.g., solar radiation, rainfall, humidity, air temperature, wind velocity is considered in the study, to estimate temperature and ground heat content of individual subsurface soil layers. A good agreement between the model predicted results and the in-situ experimental data is observed from the model validation exercise.

The model is applied to investigate ground temperature, heat capacity, and moisture distribution of a site in Warwickshire County, UK for a period of 5 years. The SGSH reserves of the test site, such as the total heat content per unit area  $\Lambda_{total}$  and the annual/seasonal/monthly net heat content per unit area  $N_{HC}$  are assessed. From the base case

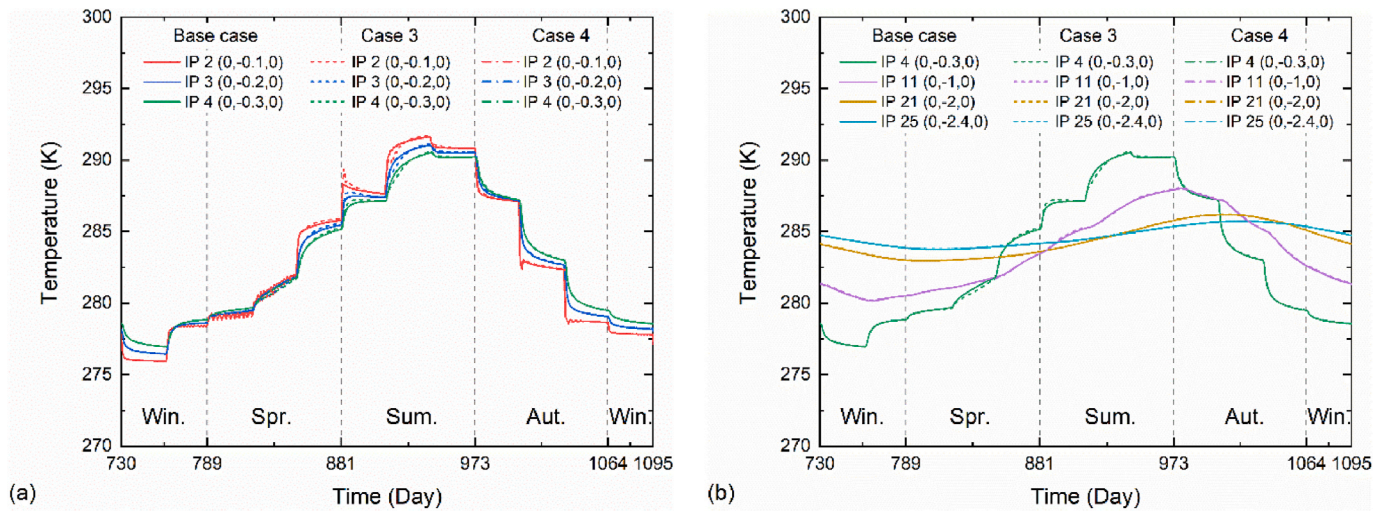


Fig. 20. Variations of temperature of inspected points in (a) Layer 1 and (b) Layer 2 of the Base case, Case 3, and Case 4.

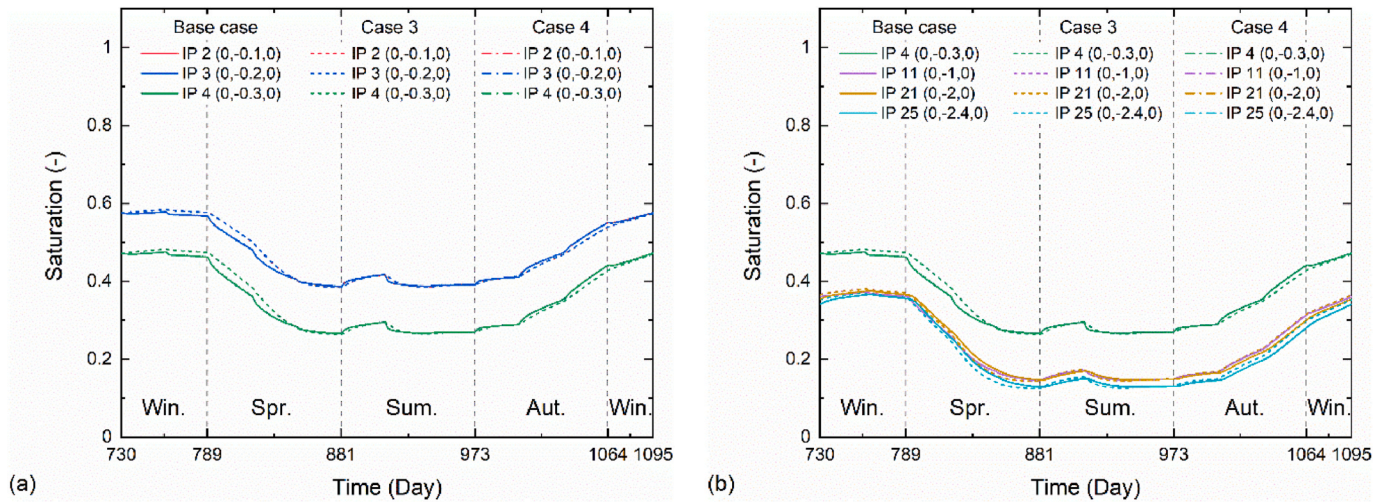


Fig. 21. Variations of saturation of inspected points in (a) Layer 1 and (b) Layer 2 of the Base case, Case 3, and Case 4.

scenario, it was found that the  $\lambda_{total}$  of the 4-m-deep domain varied from  $9.05 \times 10^7 \text{ J/m}^2$  to  $1.15 \times 10^8 \text{ J/m}^2$  and the annual  $N_{HC}$  of the 4-m-deep domain reached  $9.52 \times 10^8 \text{ J/m}^2$ . Therefore, for the test site with an area of  $200 \text{ m} \times 200 \text{ m}$ , the annual net heat storage  $N_{HS}$  can be as high as  $3.81 \times 10^{13} \text{ J}$ . This large amount of heat can be potentially used as ground source heat for building heating as environment-friendly energy.

Several scenarios where the influences of various soil layer profiles and hydraulic drainage conditions on the ground temperature, saturation, and heat content were considered, it was found that the soil types and conditions had greater impact on ground thermal potential than hydraulic drainage conditions. Improvement of soil types, in this context, could perhaps lead to enhanced ground heat capacity. For example, horizontal ground heat exchangers are not recommended in sandy soil as heat imbalance is prone to occur due to low specific heat capacity and high thermal conductivity of sand. Mixing or replacing sand with other soils with a higher specific heat capacity (e.g., clay or mudstone) can increase its heat storage potential. In addition, introducing phase change materials into the ground can also enhance its inter-seasonal heat storage capacity.

An in-depth understanding of the thermo-hydraulic behaviour of the ground is critical for realistically quantifying the annual renewable heat supply and the potential for inter-seasonal heat storage. Therefore, accurate estimation of the ground behaviour can significantly affect the

optimal design of potential heating and cooling networks and their technical and economic feasibility. In addition to the thermo-hydraulic behaviour of the ground, different types of the ground loop i.e., shallow horizontal heat collector vs. deep vertical borehole, can present significantly different characteristics. The shallow ground source heat resources of a specific site analysed using the assessment method proposed in this study can be used as a basis for the feasibility of a horizontal ground source heat pump system. The horizontal ground source heat pump system is not suitable if the shallow ground displays a negative net heat content.

Furthermore, the ground condition could have a significant impact on the CoP of a ground source heat pump supplying a district heating network, or on the supply temperature of an ambient loop heating and cooling network (i.e., 5th generation heating and cooling networks). This, consequently, affects the optimal design (e.g., size of pipes and circulation pumps) and operation of the heating and cooling networks and their life-cycle cost.

Therefore, incorporating the thermo-hydraulic behaviour of the ground in the design and operation modelling of heating and cooling networks is essential to ensure best technical and economic performance will be achieved.

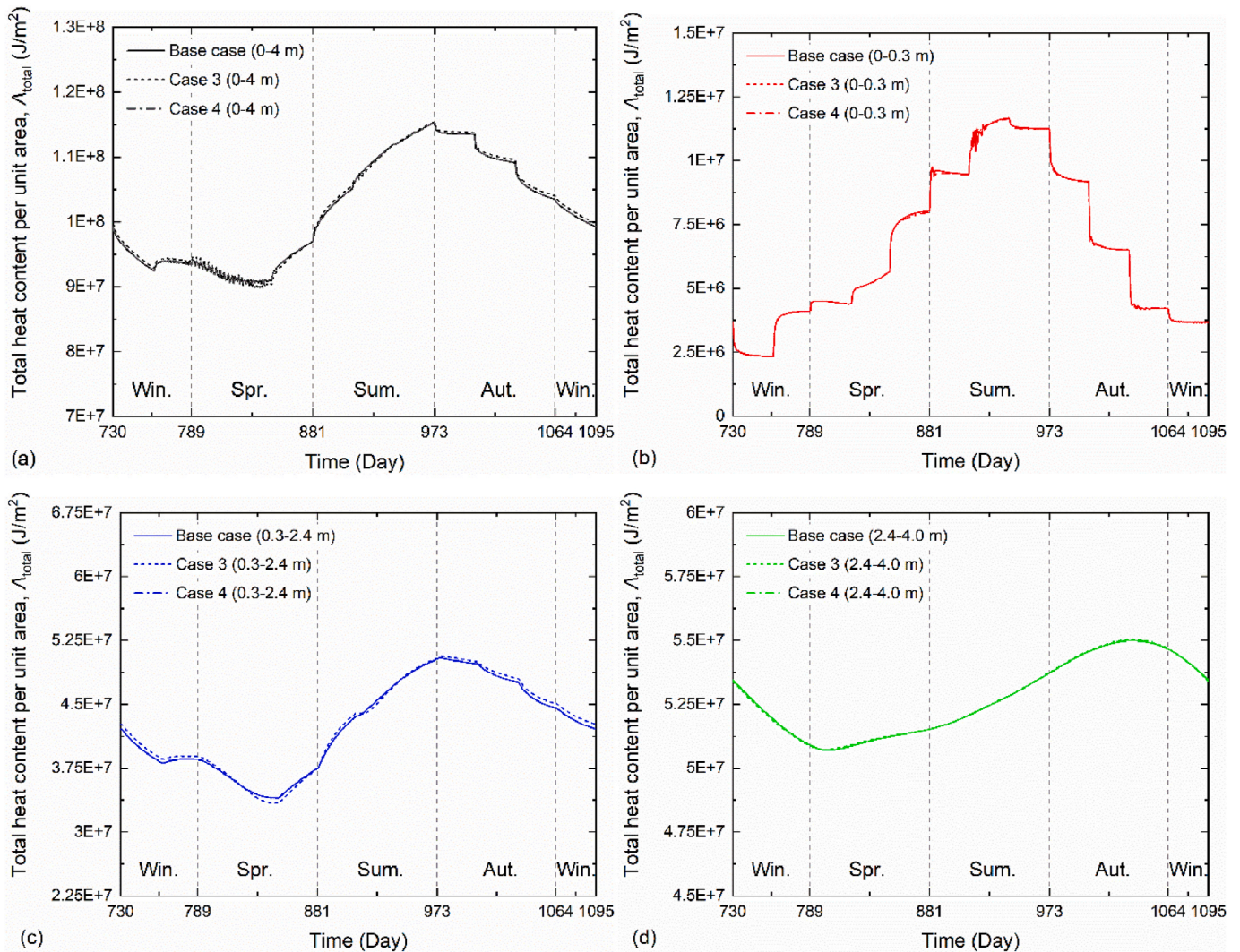


Fig. 22. Variations of total heat content per unit area for (a) the whole domain, (b) Layer 1, (c) Layer 2, and (d) Layer 3 in Year 3 of the Base case, Case 3, and Case 4.

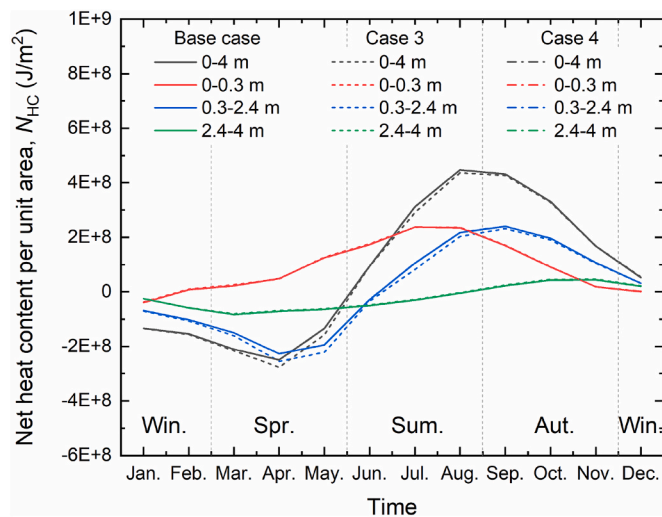


Fig. 23. Variations of monthly net heat content per unit area in Year 3 of the Base case, Case 3, and Case 4.

### Author statement

**Wu Gao:** Conceptualization, Writing - original draft & editing, Methodology, Software, Investigation. **Shakil Masum:** Conceptualization, Supervision, Project administration, Writing - review & editing. **Meysam Qadrdan:** Supervision, Project administration, Writing - review & editing, Funding acquisition. **Hywel Rhys Thomas:** Supervision, Project administration, Funding acquisition.

### Declaration of competing interest

The authors declare that they have no known competing financial interests or personal relationships that could have appeared to influence the work reported in this paper.

### Acknowledgements

This work was supported by the EPSRC funded “Integrated Heating and Cooling Networks with Heat-sharing-enabled Smart Prosumers” project (Grant number EP/T022795/1). The financial support for the authors is gratefully acknowledged.

### Appendix A. Supplementary data

Supplementary data to this article can be found online at <https://doi.org/10.1016/j.renene.2022.109788>.

org/10.1016/j.renene.2022.07.148.

## References

- [1] United Nations Framework Convention on Climate Change (UNFCCC), Report of the Conference of the Parties Serving as the Meeting of the Parties to the Paris Agreement on its Third Session, Held in Glasgow from 31 October to 13 November 2021, Conference of the Parties Serving as the Meeting of the Parties to the Paris Agreement, 2022.
- [2] European Commission (EC), A European Green Deal, 2019. [https://ec.europa.eu/info/strategy/priorities-2019-2024/european-green-deal\\_en](https://ec.europa.eu/info/strategy/priorities-2019-2024/european-green-deal_en).
- [3] International Energy Agency (IEA). <https://www.iea.org/reports/heating>, 2021.
- [4] S. Buffa, M. Cozzini, M. D'antoni, M. Baratieri, R. Fedrizzi, 5th generation district heating and cooling systems: a review of existing cases in Europe, *Renew. Sustain. Energy Rev.* 104 (2019) 504–522.
- [5] Department for Business, Energy & Industrial Strategy (BEIS), Clean Growth – Transforming Heating. Overview of Current Evidence, Department for Business, Energy & Industrial Strategy, UK, 2018.
- [6] V. Lottner, M.E. Schulz, E. Hahne, Solar-assisted district heating plants: status of the German programme Solarthermie-2000, *Sol. Energy* 69 (6) (2000) 449–459.
- [7] R.G. Bloomquist, Geothermal space heating, *Geothermics* 32 (4–6) (2003) 513–526.
- [8] B. Rezaie, M.A. Rosen, District heating and cooling: review of technology and potential enhancements, *Appl. Energy* 93 (2012) 2–10.
- [9] M. Pagani, P. Maire, W. Korosec, N. Chokani, R.S. Abhari, District heat network extension to decarbonise building stock: a bottom-up agent-based approach, *Appl. Energy* 272 (2020), 115177.
- [10] A. Prasanna, V. Dorer, N. Vetterli, Optimisation of a district energy system with a low temperature network, *Energy* 137 (2017) 632–648.
- [11] K. Bryś, T. Bryś, M.A. Sayegh, H. Ojrzynska, Subsurface shallow depth soil layers thermal potential for ground heat pumps in Poland, *Energy Build.* 165 (2018) 64–75.
- [12] K. Bryś, T. Bryś, M.A. Sayegh, H. Ojrzynska, Characteristics of heat fluxes in subsurface shallow depth soil layer as a renewable thermal source for ground coupled heat pumps, *Renew. Energy* 146 (2020) 1846–1866.
- [13] A. Dahash, F. Ochs, M.B. Janetti, W. Streicher, Advances in seasonal thermal energy storage for solar district heating applications: a critical review on large-scale hot-water tank and pit thermal energy storage systems, *Appl. Energy* 239 (2019) 296–315.
- [14] S.E. Sofyan, E. Hu, A. Kotousov, A new approach to modelling of a horizontal geohat exchanger with an internal source term, *Appl. Energy* 164 (2016) 963–971.
- [15] T. You, W. Wu, W. Shi, B. Wang, X. Li, An overview of the problems and solutions of soil thermal imbalance of ground-coupled heat pumps in cold regions, *Appl. Energy* 177 (2016) 515–536.
- [16] S.A. Oliver, H.R. Oliver, J.S. Wallace, A.M. Roberts, Soil heat flux and temperature variation with vegetation, soil type and climate, *Agric. For. Meteorol.* 39 (2–3) (1987) 257–269.
- [17] Y. Gao, S. Dong, C. Wang, Y. Chen, W. Hu, Effect of thermal intensity and initial moisture content on heat and moisture transfer in unsaturated soil, *Sustain. Cities Soc.* 55 (2020), 102069.
- [18] F. Zhu, Y. Zhou, S. Zhu, Experimental study on moisture migration in soil during coupled heat storage and release processes, *Energy Build.* 242 (2021), 110986.
- [19] G. Mihalakakou, M. Santamouris, J.O. Lewis, D.N. Asimakopoulos, On the application of the energy balance equation to predict ground temperature profiles, *Sol. Energy* 60 (3–4) (1997) 181–190.
- [20] M. Staniec, H. Nowak, The application of energy balance at the bare soil surface to predict annual soil temperature distribution, *Energy Build.* 127 (2016) 56–65.
- [21] G. Mihalakakou, On estimating soil surface temperature profiles, *Energy Build.* 34 (3) (2002) 251–259.
- [22] G.A. Akrouh, M. Sánchez, J.L. Briaud, Effect of the unsaturated soil condition on the thermal efficiency of energy piles, in: *IFCEE 2015*, 2015, pp. 1618–1627.
- [23] N. Zhang, Z. Wang, Review of soil thermal conductivity and predictive models, *Int. J. Therm. Sci.* 117 (2017) 172–183.
- [24] H.R. Thomas, Y. He, Analysis of coupled heat, moisture and air transfer in a deformable unsaturated soil, *Geotechnique* 45 (4) (1995) 677–689.
- [25] H.R. Thomas, S.W. Rees, Measured and simulated heat transfer to foundation soils, *Geotechnique* 59 (4) (2009) 365–375.
- [26] B.D.P. Hepburn, An Investigation of the Behaviour of the Ground in Response to Energy Extraction, Cardiff University, UK, 2013. Doctoral dissertation.
- [27] R.H. Brooks, A.T. Corey, Hydraulic Properties of Porous Media, Colorado State University, Fort Collins, USA, 1964, p. 3.
- [28] M.T. Van Genuchten, A closed-form equation for predicting the hydraulic conductivity of unsaturated soils, *Soil Sci. Soc. Am. J.* 44 (5) (1980) 892–898.
- [29] J.R. Philip, D.A. De Vries, Moisture movement in porous materials under temperature gradients, *Eos, Transactions American Geophysical Union* 38 (2) (1957) 222–232.
- [30] D. Krischer, H. Rohnalter, Wärmeleitung und Dampfdiffusion in feuchten Güttern, Verein Duet, Ing-Forschungsheft, 1940, p. 402.
- [31] J.R. Partington, An Advanced Treatise on Physical Chemistry: Fundamental Principles the Properties of Gases, One, Longmans, Green, 1949.
- [32] G.W.C. Kaye, T.H. Laby, Tables of Physical and Chemical Constants, Longmans, Green, 1986.
- [33] N.E. Edlefsen, A.B.C. Anderson, Thermodynamics of soil moisture, *Hilgardia* 15 (2) (1943) 31–298.
- [34] J. Ewen, H.R. Thomas, Heating unsaturated medium sand, *Geotechnique* 39 (3) (1989) 455–470.
- [35] M. Sedighi, B.D. Hepburn, H.R. Thomas, P.J. Vardon, Energy balance at the soil atmospheric interface, *Environmental Geotechnics* 5 (3) (2016) 146–157.
- [36] J.W. Deardorff, Efficient prediction of ground surface temperature and moisture, with inclusion of a layer of vegetation, *J. Geophys. Res.: Oceans* 83 (C4) (1978) 1889–1903.
- [37] J. Imberger, J.C. Patterson, A dynamic reservoir simulation model – DYRESM:5, in: H.B. Fischer (Ed.), *Transport Modes for Inland and Coastal Waters*, Academic Press, California, USA, 1981, pp. 310–361.
- [38] R.W. Lewis, P. Nithiarasu, K.N. Seetharamu, Fundamentals of the Finite Element Method for Heat and Fluid Flow, John Wiley & Sons, 2004.
- [39] S.J.R. Woodward, D.J. Barker, R.F. Zyskowski, A practical model for predicting soil water deficit in New Zealand pastures, *N. Z. J. Agric. Res.* 44 (1) (2001) 91–109.
- [40] H.U. Sverdrup, The humidity gradient over the sea surface, *J. Atmos. Sci.* 3 (1) (1946) 1–8.
- [41] I.J. Barton, A parameterization of the evaporation from nonsaturated surfaces, *J. Appl. Meteorol.* 18 (1) (1979) 43–47.
- [42] G.W. Wilson, D.G. Fredlund, S.L. Barbour, The effect of soil suction on evaporative fluxes from soil surfaces, *Can. Geotech. J.* 34 (1) (1997) 145–155.
- [43] M.D. Fredlund, J.M. Zhang, D. Tran, D.G. Fredlund, Coupling heat and moisture flow for the computation of actual evaporation, in: *Proceedings of the Canadian Geotechnical Conference and Fifth Pan-American Conference*, Toronto, Canada, 2011, October, pp. 2–6.
- [44] O.C. Zienkiewicz, R.L. Taylor, J.Z. Zhu, in: *The Finite Element Method: its Basis and Fundamentals*, sixth ed., Elsevier, 2005.
- [45] J. Douglas Jr., B.F. Jones Jr., On predictor-corrector methods for nonlinear parabolic differential equations, *J. Soc. Ind. Appl. Math.* 11 (1) (1963) 195–204.
- [46] G.S. Enrique, I. Braud, T. Jean-Louis, V. Michel, B. Pierre, C. Jean-Christophe, Modelling heat and water exchanges of fallow land covered with plant-residue mulch, *Agric. For. Meteorol.* 97 (3) (1999) 151–169.
- [47] J.C. Calvet, P. Bessemoulin, J. Noilhan, C. Berne, I. Braud, D. Courault, N. Fritz, E. Gonzalez-Sosa, J.P. Goutorbe, R. Haverkamp, G. Jaubert, MUREX: a land-surface field experiment to study the annual cycle of the energy and water budgets, *Ann. Geophys.* 17 (6) (1999) 838–854.
- [48] D. Hillel, *Applications of Soil Physics*, Elsevier, 2012.
- [49] J. Busby, A. Kingdon, J. Williams, The measured shallow temperature field in Britain, *Q. J. Eng. Geol. Hydrogeol.* 44 (3) (2011) 373–387.
- [50] W.R. Van Wijk, *Physics of Plant Environment*, North Holland Publishing Co, 1966.
- [51] British Geological Survey (BGS). <https://mapapps.bgs.ac.uk/geologyofbritain/home.html>, 2021.
- [52] Met Office (2021). <https://www.metoffice.gov.uk>.
- [53] Y.S. Song, S. Hong, Effect of clay minerals on the suction stress of unsaturated soils, *Eng. Geol.* 269 (2020), 105571.
- [54] J. Busby, Determination of thermal properties for horizontal ground collector loops, in: *Proceedings World Geothermal Congress*, Melbourne, Australia, April, 2015, pp. 19–25.
- [55] D. Parkes, J. Busby, S.J. Kemp, E. Petittler, I. Mountney, The thermal properties of the mercia mudstone group, *Q. J. Eng. Geol. Hydrogeol.* 54 (2) (2021) 1–10.
- [56] F.J. Leij, W.J. Alves, M.T. van Genuchten, J.R. Williams, The UNSODA Unsaturated Soil Hydraulic Database: User's Manual, National Risk Management Research Laboratory, Office of Research and Development, US Environmental Protection Agency, 1996.
- [57] B.C. Ball, M.F. O'Sullivan, Cultivation and nitrogen requirements for drilled and broadcast winter barley on a surface water gley (gleysol), *Soil Tillage Res.* 9 (2) (1987) 103–122.
- [58] G.A.J. Hellstrom, Ground Heat Storage: Thermal Analyses of Duct Storage Systems, Doctoral dissertation, Lund University, Sweden, 1992.
- [59] T.E. Ochsner, T.J. Sauer, R. Horton, Soil heat storage measurements in energy balance studies, *Agron. J.* 99 (1) (2007) 311.